# Phosphatidic acid induces conformational changes in Sec18 protomers that prevent SNARE priming

Received for publication, November 2, 2018, and in revised form, December 31, 2018 Published, Papers in Press, January 7, 2019, DOI 10.1074/jbc.RA118.006552

**Matthew L. Starr[‡1], Robert P. Sparks[‡1], Andres S. Arango[§1], Logan R. Hurst[‡], Zhiyu Zhao[§], Muyun Lihan[§], Jermaine L. Jenkins[¶], Emad Tajkhorshid[‡§‖], and Rutilio A. Fratti[‡§2]**

*From the [‡]Department of Biochemistry, University of Illinois at Urbana-Champaign, Urbana, Illinois 61801, the [§]Center for Biophysics and Quantitative Biology, University of Illinois at Urbana-Champaign, Urbana, Illinois 61801, the [‖]Beckman Institute for Advanced Science and Technology, University of Illinois at Urbana-Champaign, Urbana, Illinois 61801, and the [¶]Department of Pathology and Laboratory Medicine, University of Rochester Medical Center, Rochester, New York 14642*

Edited by Phyllis I. Hanson

**Eukaryotic cell homeostasis requires transfer of cellular components among organelles and relies on membrane fusion catalyzed by SNARE proteins. Inactive SNARE bundles are reactivated by hexameric *N*-ethylmaleimide-sensitive factor, vesicle-fusing ATPase (Sec18/NSF)-driven disassembly that enables a new round of membrane fusion. We previously found that phosphatidic acid (PA) binds Sec18 and thereby sequesters it from SNAREs and that PA dephosphorylation dissociates Sec18 from the membrane, allowing it to engage SNARE complexes. We now report that PA also induces conformational changes in Sec18 protomers and that hexameric Sec18 cannot bind PA membranes. Molecular dynamics (MD) analyses revealed that the D1 and D2 domains of Sec18 contain PA-binding sites and that the residues needed for PA binding are masked in hexameric Sec18. Importantly, these simulations also disclosed that a major conformational change occurs in the linker region between the D1 and D2 domains, which is distinct from the conformational changes that occur in hexameric Sec18 during SNARE priming. Together, these findings indicate that PA regulates Sec18 function by altering its architecture and stabilizing membrane-bound Sec18 protomers.**

Membrane fusion is necessary for all eukaryotes to effectively transport cellular components between organelles. The trafficking and fusion of vesicles is carried out through a series of events that are highly conserved across eukarya (1). Although many proteins that drive the process may differ between eukaryotic species, they all perform similar roles allowing compartment contact, bilayer fusion, and luminal content mixing (2). The final stage of membrane fusion, and luminal content mixing, is catalyzed by SNARE[3] proteins. Each participating membrane contributes either an R-SNARE or three Q-SNARE coils that wrap around each other to form a parallel four-helical *trans*-SNARE complex that brings membranes into close apposition. The formation of such complexes releases free energy that is transmitted to the membranes to trigger fusion. Once fusion occurs and membranes are merged, the four-helical SNARE bundle, now a *cis*-SNARE complex, is inactive and requires disassembly to undergo a new round of fusion.

The disassembly of *cis*-SNAREs, also known as *Priming*, is carried out by the $AAA^+$ protein Sec18/NSF and its adaptor protein Sec17/$\alpha$-SNAP (3) (Fig. 1*A*). Current models suggest that NSF primes *cis*-SNAREs through a "loaded spring" mechanism triggered by *cis*-SNARE recognition and ATP hydrolysis (4). NSF binds to *cis*-SNAREs with the help of $\alpha$-SNAP to form what is known as the 20S complex (5–8). Although NSF was originally isolated as a trimer or tetramer, it can only prime SNAREs as a homohexamer that surrounds the *cis*-SNAREs and $\alpha$-SNAP proteins to form the 20S particle (9–11). Association with *cis*-SNARE–$\alpha$-SNAP complexes triggers ATP hydrolysis, which leads to a large conformational change in the protein, with the major change occurring at the N terminus where it folds back over the D1–D2 rings (8). This generates enough force to disrupt the 20S complex and separate the individual SNAREs from each other effectively reactivating them.

Previous work identified that both NSF and Sec18 bind to the regulatory glycerophospholipid phosphatidic acid (PA) (12, 13). PA has been shown to have regulatory effects in multiple vesicular trafficking pathways including sporulation, regulated

This work was supported by National Institutes of Health Grants R01-GM101132 (to R. A. F.), and P41-GM104601, U01-GM111251, and U54-GM087519 (to E. T.), National Science Foundation Grant MCB 1818310 (to R. A. F.), and the Office of Naval Research ONR Grant N00014-16-1-2535 (to E. T.). The authors declare that they have no conflicts of interest with the contents of this article. The content is solely the responsibility of the authors and does not necessarily represent the official views of the National Institutes of Health.

This article contains Videos S1–S4.

[1] These authors contributed equally to the results of this work.

[2] To whom correspondence should be addressed: Dept. of Biochemistry, University of Illinois at Urbana-Champaign, Urbana, IL 61801. E-mail: rfratti@illinois.edu.

[3] The abbreviations used are: SNARE, soluble *N*-ethylmaleimide-sensitive factor attachment protein receptor; $diC_8$, dioctanoyl; PA, phosphatidic acid; DAG, diacylglycerol; PC, phosphatidylcholine; PE, phosphatidylethanolamine; PS, phosphatidylserine; MSP, membrane scaffold protein; NEM, *N*-ethylmaleimide; NSF, NEM-sensitive factor; $\alpha$-SNAP, soluble NSF adaptor protein; YPD, yeast extract/peptone/dextrose; MST, microscale thermophoresis; Ni-NTA, nickel-nitrilotriacetic acid; NBD, nucleotide-binding domain; SPR, surface plasmon resonance; ND, nanodiscs; GST, glutathione *S*-transferase; ANS, 8-anilino-1-naphthalenesulfonic acid; MD, molecular dynamics; r.m.s. deviation, root mean square deviation; PDB, Protein Data Bank; POPA, 1-palmitoyl-2-oleoyl-*sn*-glycero-3-phosphate; POPC, 1-palmitoyl-2-oleoyl-*sn*-glycero-3-phosphatidylcholine; POPE, 1-palmitoyl-2-oleoyl-*sn*-glycero-3-phosphatidylethanolamine; C8-PA, 1,2-dioctanoyl-*sn*-glycero-3-phosphate; C8-DAG, 1,2-dioctanoyl-*sn*-glycerol; C8-PS, 1,2-dioctanoyl-*sn*-glycero-3-phospho-L-serine; PMSF, phenylmethylsulfonyl fluoride; AIM, autoinducing medium; MBP, maltose-binding protein; DEP, Dishevelled, Egl-10, and pleckstein domain.

exocytosis, lysosomal maturation, and homotypic vacuole fusion (13–17). PA production through phospholipase D activity promotes the exocytosis of secretory granules in chromaffin and PC-12 cells (18–21), as well as Glut4 containing vesicles in adipocytes (22). The ability of PA to promote fusion in these systems is attributed to inducing negative membrane curvature (23), binding SNAREs (24, 25), and promoting hemifusion (21, 26).

PA production, however, is not always a positive signal for fusion. In the case of Sec18, increased PA levels lead to reduced priming activity likely due to a decrease in recruitment to *cis*-SNAREs (13). On yeast vacuoles, PA is converted to diacylglycerol (DAG) by the PA phosphatase Pah1, an ortholog of mammalian Lipin1. In the absence of Pah1 activity, PA levels remain intact and sequester Sec18 from *cis*-SNARE complexes to prevent priming and arrest the fusion pathway, whereas deleting the other PA yeast phosphatases had no effect on fusion (17). DAG can be converted to PA through the action of the DAG kinase Dgk1, whose inactivation leads to elevated DAG concentrations that enhance fusion through modulating the activity of the Rab GTPase Ypt7 (27). Thus, the interconversion of PA and DAG serves as a regulatory switch to control vacuole fusion.

Here we asked what effects PA binding has on the overall architectural dynamics of Sec18 that could lead to a decrease in its priming activity. To do so, we measured binding of monomeric and hexameric Sec18 to different forms of PA. We report that monomeric Sec18 has significantly stronger binding than the hexameric form to all forms of PA. We probed changes to the architecture of Sec18 when bound to short-chain PA and found that the protein exists in a significantly different conformation in its PA-bound state, without significant changes to its secondary structure. To study the mechanism of Sec18 binding to PA, molecular dynamics simulations were performed using the mammalian version of Sec18, namely NSF. NSF was used as it has high identity to Sec18 and has more structural information available at the Protein Data Bank (PDB ID 3J94) (28). The molecular dynamic simulations performed suggest NSF binds to PA at regions of the protein that are only exposed in the monomeric state of the protein. Taken together, we propose that PA regulates the priming activity of NSF/Sec18 by limiting the formation of its active hexamer.

## Results

### *Sec18 monomer binds to PA with higher affinity than the hexameric form*

Our previous work showed that Sec18 preferentially bound to liposomes containing phosphatidylcholine (PC), phosphatidylethanolamine (PE), and PA relative to those composed of only PC and PE, or ones where PA was replaced with DAG or phosphatidylserine (PS) (13). This was in keeping with older findings showing that mammalian NSF bound to resin-linked PA (12). Here our studies were extended to further define how Sec18 binds to PA. To start we used microscale thermophoresis (MST) to acquire binding affinities to dioctanoyl-PA (C8-PA), which prevents Sec18 from binding *cis*-SNARE complexes, consequently precluding priming from occurring (13). We used both monomeric and hexameric Sec18 with a range of C8-PA. The C-terminal $His_8$ tag of Sec18 was labeled with Ni-NTA Atto 488. As shown in Fig. 1*B*, monomeric Sec18 (mSec18) bound to C8-PA with a $K_D$ of 1.4 ± 0.68 $\mu$M, whereas the hexameric form (hSec18) had a $K_D$ of 29 ± 8.6 $\mu$M. This suggested that either hSec18 has residues occluded for PA binding or is in a suboptimal conformation to efficiently bind C8-PA. It is possible that a small soluble C8-PA could access a binding site on Sec18 that is obscured in the hexamer, whereas membranous long-chain PA is unable to reach PA-binding regions on Sec18 hexamers, especially regions contained in the hexamerization interface of Sec18 holoenzyme.

Due to the difference in binding affinities to C8-PA, we next asked if limiting the mobility of PA to two dimensions would show a similar disparity between the monomer and hexamer. To this aim we used extruded 0.8-$\mu$m diameter liposomes to approximate the diameter of yeast vacuoles. We found that mSec18 bound 0.8 $\mu$M liposomes containing 10% long-chain PA (80% POPC, 10% POPE) with a $K_D$ of 29 ± 20 $\mu$M, whereas hSec18 bound these liposomes poorly with a $K_D$ of 423 ± 215 $\mu$M (Fig. 1, *C* and *D*). We next used PC liposomes as a negative control and found that hSec18 bound as poorly as it did to PA liposomes, whereas mSec18 lacked any detectable interactions above the background noise of the system. These findings further establish that hexameric Sec18 lacks the ability to bind PA, potentially by masking a binding site or by restricting conformational changes needed to bind PA.

### *Sec18 binding to PA is specific*

Our previous work showed that Sec18 binds to vacuoles in a PA-dependent manner (13). However, others have shown that proteins with PA binding capabilities sometimes associate with other anionic lipids including phosphoinositides and phosphatidylserine (PS) in a nonspecific, charge-dependent manner (29). We previously observed that Sec18 does not associate with PS in the membrane, however, we wanted to additionally verify that its membrane association was not due to highly anionic phosphoinositides. Here we show that Sec18 does not readily bind to C8-PI(4,5)$P_2$ ($K_D \geq 350$ $\mu$M) (Fig. 1*C*). This is significant because it was previously shown that PI(4,5)$P_2$ is required for SNARE priming to occur at the vacuole (30). Our results show that Sec18 association with lipids at the vacuole membrane is PA specific.

### *ATP blocks PA binding by Sec18*

Sec18/NSF, like many other $AAA^+$ proteins contains two nucleotide-binding domains (NBD) each residing in a one of the domains that make up the rings of the hexameric protein. The D1 ring of Sec18 hydrolyzes ATP to generate the mechanical force needed to disrupt *cis*-SNARE bundles, whereas the D2 ring binds ATP to stabilize the hexameric form of the protein. This is reflected in the different affinities for ATP found between the two NBDs. In NSF the D1 NBD binds ATP with a $K_D$ of 15–20 $\mu$M, whereas the D2 NBD binds with a $K_D$ of 30–40 nM (31). Here we asked if ATP binding would affect PA binding. We added 1 mM ATP-$Mg^{2+}$ to binding assays with Sec18 and 0.8-$\mu$m PA liposomes. We found that ATP-$Mg^{2+}$ reduced mSec18 binding to PA liposomes, whereas not affecting the already poor binding by hSec18 (Fig. 1, *D* and *E*). The effect of ATP on mSec18 was possibly due to hexamerization of the protein and reduced masking of the PA-binding site. Interestingly,

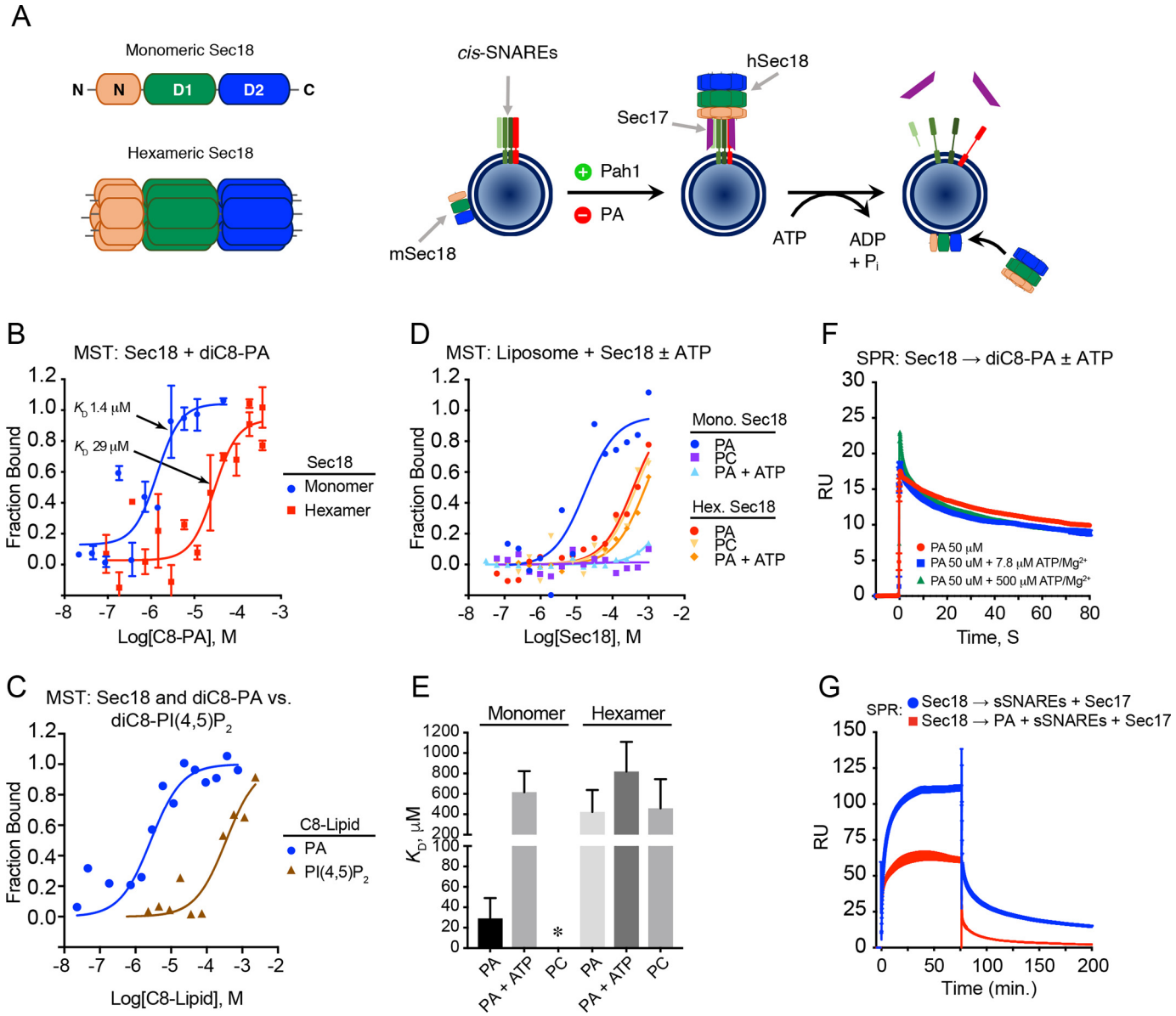


**Figure 1. Sec18 hexamer and monomer binding affinity for PA.** *A,* schematic of Sec18 monomer and hexamer. Shown is the priming reaction where monomeric Sec18 (*mSec18*) is initially bound to the membrane after which it is released upon Pah1 activity. Released mSec18 then forms hexameric Sec18 (*hSec18*) and is recruited to *cis*-SNARE bundles decorated with Sec17. Sec18 hydrolyzes ATP to dissociate the SNAREs into individual proteins leading the release of Sec17 and the soluble SNARE Vam7. *B,* C8-PA MST measurements were performed using purified Sec18 monomer and hexamer labeled with Ni-NTA Atto 488 dye at 90% LED and High MST using NT.115 labeled thermophoresis. Binding affinity was measured using thermophoresis at 15 s by mixing separate reactions of half 100 nM Atto 488-labeled Sec18 monomer and half 1:1 titrations of C8-PA with the highest concentration (370 $\mu$M) according to the GraphPad Sigmoidal 4PL curve. *C,* MST measurements of monomeric Sec18 with C8-PA *versus* C8-PI(4,5)$P_2$. *D,* the effect of 1 mM ATP-$Mg^{2+}$ Sec18 binding to liposomes. 800-nm diameter extruded PA liposomes (10% PA, 70% PC, and 20% PE) and PC liposomes (80% PC, 20% PE) were incubated with Sec18 monomer or hexamer in the presence or absence of ATP. *E,* the quantitation of multiple experiments run in *panel D*. *Asterisk* (*), no measureable PC-liposome binding was detected above the background noise of the system. *F,* SPR of ATP competition of soluble C8-PA binding to Sec18. *G,* SPR of Sec18–$His_8$ bound to CM5 sensor chips. Soluble SNARE complexes (167 nM) (lacking transmembrane domains) decorated with 500 nM Sec17 at a 3:1 ratio were flowed over the bound Sec18 in the presence or absence of 1.25 $\mu$M C8-PA. $n \geq 3$ for all data shown.

ATP had no effect on the interaction of mSec18 and C8-PA (Fig. 1*F*). The difference could be due to the close apposition of mSec18 to the membrane that affects how ATP alters PA binding, which is not recapitulated in solution.

### *PA blocks Sec18 binding to Sec17–SNARE complexes*

Previously we showed that C8-PA inhibits priming activity on isolated vacuoles and by preventing its association with SNAREs. To see the direct effect on protein complex formation we used surface plasmon resonance (SPR). Sec18 was linked to Ni-NTA sensor chips through its C-terminal $His_8$ tag. For these experiments we used pre-assembled soluble SNARE bundles in which the transmembrane domains were deleted from Vam3, Vti1, and Nyv1. The soluble SNAREs were mixed with the naturally soluble SNARE Vam7 to allow for 4-helical bundle formation as described previously (32, 33). Soluble SNARE bundles were mixed with recombinant Sec17 and flowed over Ni-NTA-bound Sec18. This approach showed 100 response units. However, when C8-PA was added in the mixtures with the SNAREs and Sec17, we observed a 50% reduction in

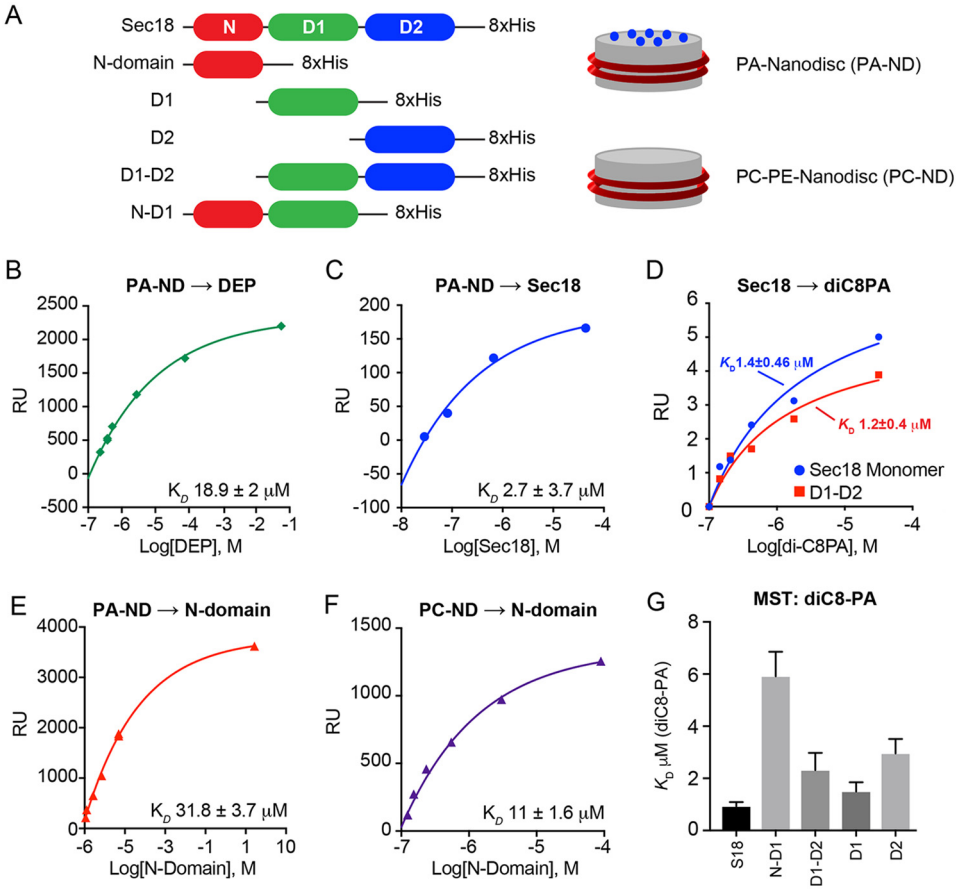


**Figure 2. Sec18 binding affinity compared with DEP PA-binding domain for PA nanodiscs.** *A,* schematic of Sec18 constructs and nanodiscs containing PC:PE:PA (80:15:5) (*PA-ND*) or PC:PE (80:20) alone (*PC-ND*). *Red* bands depict the membrane scaffold proteins, whereas the *gray* represent the lipid bilayer. The *blue spheres* symbolize the presence of PA. *B,* GST–DEP was flowed over PA-ND attached to a Ni-NTA chip using a BIAcore T200 with a flow rate of 20 μl/s. The steady state fit was exported from BIAevaluate software to GraphPad at 4 s before injection stop set at 90 s with disassociation of 120 s. *C,* SPR analysis of GST–Sec18 monomer with PA-ND. *D,* SPR of Sec18 –$His_8$ or D1–D2–$His_8$ bound to a Ni-NTA chip with C8-PA. *E,* SPR analysis of GST–N-domain with PA-ND. *F,* SPR analysis of GST–N-domain with PC-ND. *G,* MST performed with mSec18, N–D1, D1–D2, D1, and D2 constructs. The $His_8$ tags were labeled with 100 nM Ni-NTA Atto 488 and binding was measured using 90% LED and 60% MST. M.O. Affinity analysis software was used and thermophoresis exported at 15 s. $n = 3$ for all data shown. *RU*, response unit.

response units (Fig. 1*G*). Because SPR response units are based on mass, we conclude that PA blocked the assembly of the larger SNARE–Sec17–sSNARE complex.

### *Both D1 and D2 domains bind Sec18*

Based on structural predictions for PA binding (see below), we hypothesized that Sec18 binds PA using both its D1 and D2 domains. To test this, we compared full-length Sec18 with domains or protein truncations lacking the N-terminal domain (D1–D2) or the D2 domain (N–D1) (Fig. 2*A*). Using SPR, GST–Sec18 constructs were flowed over nanodiscs (ND) containing long-chain PC and PE (80:20) or long-chain PC, PE, and PA (80:15:5). The ND were linked to the Ni-NTA chip through the His tags of the membrane scaffold proteins. First we tested the known PA-binding domain DEP of the murine protein Dvl2 (34). GST–DEP bound to PA-ND with a $K_D$ of 18.9 ± 2 μM (Fig. 2*B*). Next we tested binding of full-length GST–Sec18 to PA-ND and found that it bound with a $K_D$ of 2.7 ± 2 μM, illustrating that Sec18 interacted with PA as well or better than the *bona fide* PA-binding domain DEP (Fig. 2*C*). To verify that the GST tag did not alter the binding of Sec18 to PA, we linked Sec18 –$His_8$ to the sensor chip and flowed C8-PA. By this approach we measured a $K_D$ of 1.4 ± 0.46 μM, illustrating that the GST tag had no effect on PA binding (Fig. 2*D*). In parallel we tested the D1–D2 construct, lacking the N-terminal domain, and found that it bound PA with nearly identical affinity ($K_D$, 1.2 ± 0.4 μM) to full-length Sec18. Because the Sec18 N-domain has a polybasic surface at its Sec17-binding site, we tested if it also bound to long-chain PA. We found that the N-domain bound poorly to PA-ND with a $K_D$ of 31.8 ± 3.7 μM and to PC-ND with a $K_D$ of 11 ± 1.6 μM (Fig. 2, *E* and *F*). These data suggest that the N-domain has no lipid-binding specificity and that the effect of PA on Sec18 is limited to the D1–D2 domains. Next, we used MST to verify our SPR data and to further examine PA binding by various constructs. In Fig. 2*G*, we show that full-length Sec18 bound C8-PA with a $K_D$ of 0.927 ± 0.161 μM, which was similar to the value we observed with SPR. We next tested the individual domains. The individual D1 and D2 domains bound PA with $K_D$ values 1.5 ± 0.35 and 2.96 ± 0.55 μM, respectively, which is near to what we saw with the D1–D2 construct. In comparison, the N–D1 construct bound PA poorly relative to the D1 construct. This suggested that the N-domain could sterically interfere with PA binding or perhaps induce a suboptimal lipid-binding conformation in D1 that does not occur in the full-length protein.

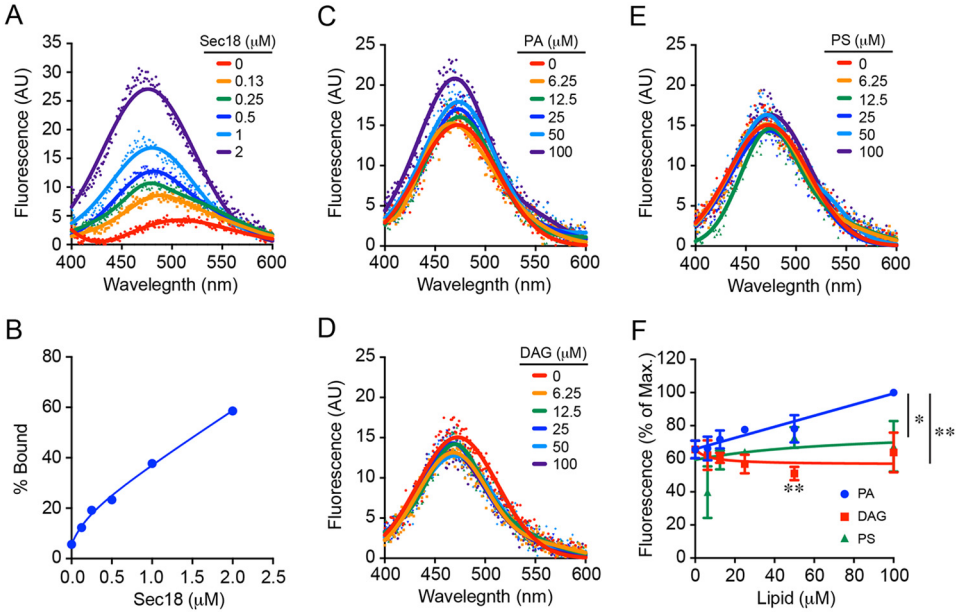


**Figure 3. C8-PA acid alters the binding of 1,8-ANS to Sec18.** Increasing concentrations of Sec18–$His_8$ were incubated with ANS (5 $\mu$M) in assay buffer and a representative fluorescence spectrum (excitation 390, emission 400–600 nm) is shown (*A*). Relative fluorescence at 460 nm (*B*). Sec18–$His_8$ (0.5 $\mu$M) was incubated with increasing concentrations of short-chain lipids in the presence of ANS (5 $\mu$M) and fluorescence spectra were taken. A representative spectrum for each lipid tested is shown: C8-PA (*C*), C8-DAG (*D*), and C8-PS (*E*). *F*, maximum fluorescence for each lipid concentration was normalized against overall maximum fluorescence (100 $\mu$M C8-PA) for relative comparison. $n = 3$ for all data shown. *, $p < 0.05$; ** $p < 0.01$; ***, $p < 0.001$.

### *Phosphatidic acid alters the conformation of Sec18*

Our data thus far suggests that Sec18 undergoes conformational changes that allow mSec18 to bind PA, whereas hSec18 lacks the ability to bind the lipid. To further probe for conformational changes to Sec18 we tested whether PA significantly alters binding of 8-anilino-1-naphthalenesulfonic acid (ANS) to mSec18. ANS is a dye that has been extensively used to test lipid-binding proteins because it associates with solution-exposed hydrophobic motifs (35, 36). Binding of ANS to a protein results in an increase in fluorescence yield and a blue-shifted emission. Because we have previously seen PA binding to mSec18 we expected ANS to also bind the protein in our assay. As expected, we observed ANS binding to mSec18 in a dose-dependent fashion (Fig. 3, *A* and *B*). We next wanted to test for any conformational changes upon PA binding that altered ANS binding to Sec18. To do this, we titrated increasing amounts of C8-PA into our assay and measured changes in the ANS fluorescence spectra. Because C8-PA is partially hydrophobic, ANS was first incubated with each lipid concentration to obtain a background spectrum before protein was then added to the assay, and fluorescence was again measured. The difference spectra from these measurements shows that addition of C8-PA increases the binding of ANS to Sec18 (Fig. 3, *C* and *F*). To confirm that the changes in ANS fluorescence were specific to PA binding, we tested the addition of DAG, the product of Pah1 activity on PA. No change in ANS fluorescence was detected in the presence of C8-DAG, which is consistent with the inability of Sec18 to bind to DAG (Fig. 3, *D* and *F*). We also tested the anionic lipid phosphatidylserine (PS). Similar to what we observed with DAG, the addition of C8-PS had no effect on ANS fluorescence (Fig. 3, *E* and *F*). Together these data suggest that C8-PA binding to Sec18 results in a conformational change in the protein that exposes additional hydrophobic pockets to solution. Such a change may account for the differences previously seen in Sec18 priming activity and *cis*-SNARE association (13).

To further probe for conformational changes to Sec18 induced by PA we utilized a limited proteolysis assay. Proteins can exhibit differences in their proteolytic cleavage profiles when bound to a ligand that significantly changes their overall architecture (35). Because we observed an increase in solution-exposed regions of Sec18 in the presence of PA, *i.e.* increased ANS fluorescence, we expected to also see an increased sensitivity to protease degradation in the same conditions. To measure this, mSec18 was incubated with increasing concentrations of trypsin with and without C8-PA addition. As expected, mSec18 sensitivity to trypsin degradation increased in the presence of C8-PA, whereas the presence of DAG had no effect (Fig. 4, *A* and *B*).

Additionally, we performed the same limited proteolysis assay using thrombin in place of trypsin. Thrombin displays much higher specificity than trypsin and should only cleave proteins at specific recognition sites. Incubation of Sec18 with thrombin alone showed no proteolytic degradation of the protein, indicating that no recognition sites were accessible to the protease. However, upon addition of C8-PA thrombin was able to cleave Sec18 (Fig. 4, *C* and *D*). Once again, inclusion of C8-DAG did not show a similar effect indicating once again that the observed conformation change was PA specific. Finally, we titrated C8-PA into a thrombin cleavage assay keeping the concentration of the protease constant. Cleavage of Sec18 by thrombin showed dose dependence for C8-PA (not shown). These data illustrate that C8-PA binding to Sec18 alters the conformation of the protein allowing for the exposure of an otherwise shielded thrombin-recognition site. Sec18 has one predicted thrombin-recognition site (after Arg-638), which is

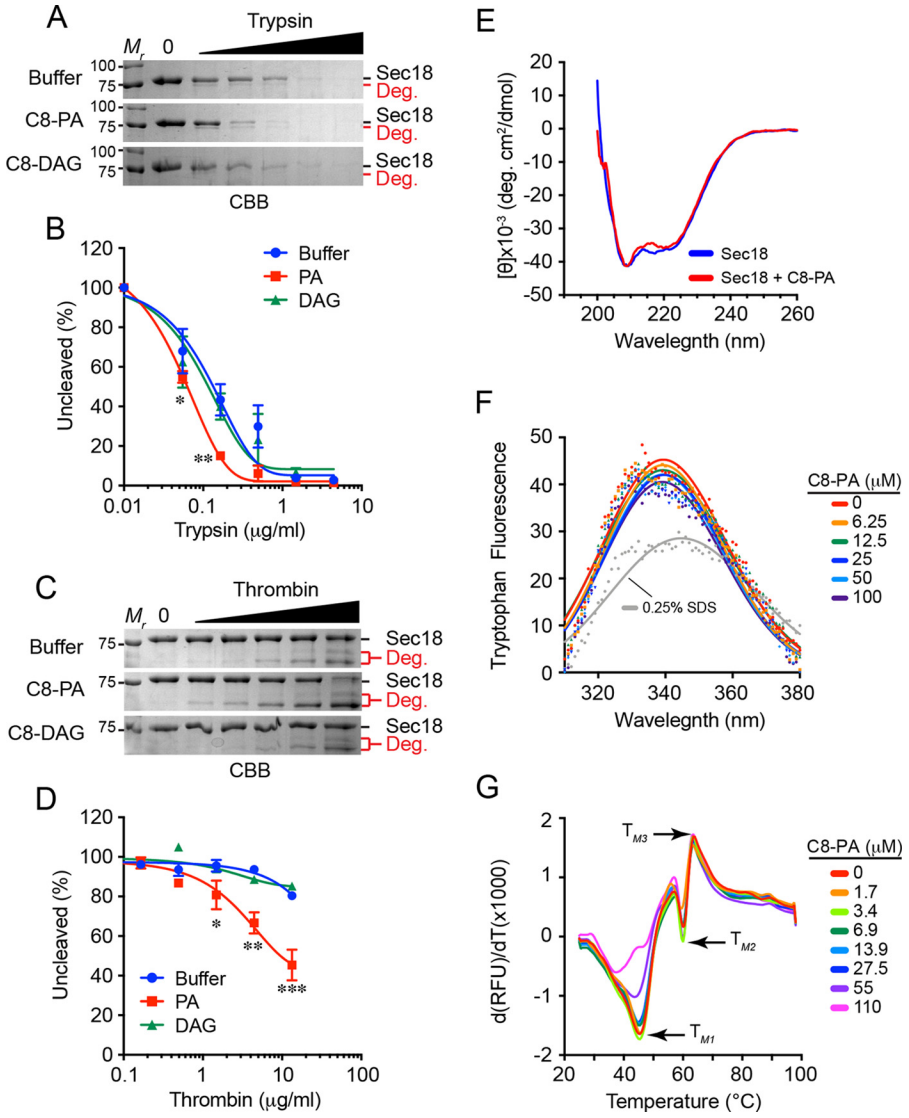


**Figure 4. C8-PA alters the proteolytic cleavage profile of Sec18, but does not affect secondary protein structure.** Sec18–$His_8$ was incubated with C8-PA, C8-DAG, or alone before incubation with increasing concentrations of trypsin (*A*) or thrombin (*C*). Densitometry values of the un-cleaved band were measured for each concentration and normalized against the input lane for trypsin (*B*) and thrombin (*D*). *Deg.*, degradation products. *E,* CD spectra were measured (260 to 200 nm, 50 nm $min^{-1}$) for Sec18–$His_8$ in the presence and absence of C8-PA (100 $\mu$M). *F,* intrinsic tryptophan fluorescence was measured with Sec18–$His_8$ (500 nM) incubated with increasing concentrations of C8-PA and fluorescence spectra were measured (excitation 295, emission 300–400 nm). The fluorescence (emission 333 nm) for each concentration tested was normalized against the no lipid control and is shown. SDS (0.25%) was used as a control for changing tryptophan fluorescence upon loss of secondary structure. *G,* differential scanning fluorimetry first derivative melting curves were measured (SYPRO orange: excitation 490, emission 560 nm) for increasing concentrations of C8-PA. $n = 3$ for all data shown. $M_r$, relative molecular mass markers. *, $p < 0.05$; **, $p < 0.01$; ***, $p < 0.001$.

located in the D2 domain of the protein (exPASy). The D2 domain is responsible for the multimerization of Sec18 to its active hexamer when it is in a nucleotide-bound state (37, 38). This further suggests that PA alters the conformation of the Sec18 D2 domain, or potentially the conformation of D2 with respect to D1 allowing binding to PA. Changes to the D2 domain structure could alter nucleotide binding or disrupt key interactions between protomers thereby decreasing Sec18 hexamer formation. Sec18 is known to associate with *cis*-SNAREs in its active hexameric form, so inhibition of hexamer formation could decrease its ability to properly recruit to inactive SNARE complexes. This idea is consistent with previous observations that showed increased PA at the vacuole led to decreased recruitment of Sec18 to *cis*-SNARE complexes (13).

### *Phosphatidic acid has no significant effect on the secondary structure of Sec18*

Because we observed significant changes in the conformation of Sec18 upon binding to C8-PA we next wanted to monitor changes in the secondary structure of the protein when bound to the lipid. To do this we observed the $\alpha$-helix and $\beta$-sheet content of Sec18 in the presence of PA using circular dichroism (CD). CD spectra of mSec18 were obtained in the absence and presence of C8-PA to determine if the protein's secondary structure was significantly affected by binding the lipid. The CD spectrum obtained for mSec18 alone showed that the protein was well folded (Fig. 4*E*). Upon addition of C8-PA, no significant changes were seen in the

spectrum suggesting the lipid binding does not alter secondary structure features within the protein.

To rule out any denaturation caused by binding of C8-PA to Sec18, intrinsic tryptophan fluorescence was measured with and without lipid addition. Sec18 contains three tryptophan residues (Trp-88, Trp-91, and Trp-632) in its N and D2 domains. Upon denaturation of Sec18 with SDS, Trp fluorescence was red-shifted and showed decreased intensity (Fig. 4*F*). Upon incubation with C8-PA, no shift or intensity change was observed. This suggests that PA binding to Sec18 did not lead to denaturation, *i.e.* causing a conformational change large enough to alter the local environment of any of the Trp residues found in the protein.

Finally, to test whether binding PA altered the thermal stability of Sec18, we used differential scanning fluorimetry (39). Sec18 was labeled with SYPRO orange dye, incubated with different concentrations of C8-PA in separate wells, and equilibrated prior to starting a melting curve. Fluorescence was scanned across a temperature gradient of 20 to 95 °C and the first derivative of the fluorescence data were used to determine the $T_m$ for each condition. Differential scanning fluorimetry has the ability to show multiple melting transitions (40, 41). Our data show that mSec18 has three melting transitions. The first mSec18 transition ($T_{M1}$) occurred at ~45 °C, whereas $T_{M2}$ and $T_{M3}$ were at 60 and 64 °C, respectively (Fig. 4*G*). The addition of C8-PA had no effect on $T_{M2}$ and $T_{M3}$, as the curves overlapped with the that of apo-Sec18. That said, C8-PA has a striking effect at $T_{M1}$ where we observed a dose-dependent increase in fluorescence. This likely mirrors the conformational changes seen with limited proteolysis and ANS fluorescence. Taken together these observations lead us to conclude that PA binding to Sec18 induces a significant change to the architecture of the protein but does not denature the protein nonspecifically.

### *NSF D1–D2 undergoes large conformational change during transition between hexameric and monomeric forms*

To examine the Sec18 conformational changes we observed previously at a more detailed level, atomic molecular dynamics (MD) simulations were performed using NSF, the mammalian homolog of Sec18. The NSF D1–D2 monomer extracted from the cryo-EM structure of an ATP-bound NSF complex (PDB 3J94) after removing bound ATPs was equilibrated with restraints for 20 ns and then relaxed for 200 ns (Video S1). Based on the overall $\alpha$ carbon (C$\alpha$) r.m.s. deviation, the monomer undergoes conformational changes up to 15 Å apart from the form originally adopted in the hexamer (Fig. 5*A*). Calculation on the secondary structure components showed that only the modeled loop region from residue 458 to 478 transitioned from the helix during the relaxation to turn and coil (data not shown). This is expected as the loop was poorly resolved in cryo-EM and was only stabilized by interactions with the N-domain in the template crystal structure (the N–D1 domain of p97) used in homology modeling. The stable secondary structure observed in D1 and D2 domains indicated that the large deviation did not come from secondary structural changes, further verifying CD experiments. Instead, we observed that the conformational change was accompanied by an opening-up process of D1 and D2 domains during the relaxation. The observation was in agreement with the hypothesis that NSF hexamerization might require certain conformations of D1–D2 monomer and that the conformation required could be further stabilized at the hexamer interface. Fig. 5*B* shows the equilibration of individual protomers in a NSF hexamer. These data indicate that the hexamer is more stable (Video S2).

### *Residues of NSF shown to bind to C8-PA are not available for PA binding when it is in the hexameric form*

Computational flooding studies were performed for both monomeric and hexameric forms of the NSF D1–D2 domains, based on the structural information of mammalian NSF (Fig. 6*A*). The binding affinity of each amino acid residue was analyzed using percent bound as determined by the fraction of time when PA lipids were found in proximity (minimal distance between phosphate group atoms of PA and the amino acid residue below H-bond distance). Residues determined to have highest percent bound were determined for both monomeric and hexameric forms of D1–D2. Our flooding simulations of NSF hexamer showed that residues having the highest percent bound PA in the monomer (Fig. 6*B*) were shielded to block lipid binding in the hexameric NSF D1–D2 construct (Fig. 6*C*). This suggests that PA binding specificity lies somewhere within the hexameric interface.

### *Binding prediction and clustering analysis of PA-binding regions of NSF*

Ensemble molecular docking of C8-PA to NSF monomer was performed using the aforementioned D1–D2 equilibrium simulation (42). Snapshots from the equilibrium trajectory were utilized for molecular docking every 100 ps to fully sample conformational dynamics. The resulting docked C8-PA poses were clustered (43) and an average Autodock Vina scoring function scores were determined for the clusters of monomeric NSF. These scoring function results show some correlation with the MST binding measurements of mSec18 and hSec18 to C8-PA (44) (Fig. 7, *A* and *E*). To further verify the cluster analysis, a SiteMap analysis was performed and the top three site scores were chosen (Fig. 7*D*). Both Fig. 6, *A* and *D,* indicate affinity to two main regions of Sec18, mainly in the interface of D1 and D2, as well as a significant affinity to the D2 ATP-binding site (Fig. 7, *B* and *C*). Furthermore, to fully evaluate the potential PA-binding sites of Sec18, the hexameric form was also surveyed, using the same methodology as the monomer. The results showed a preferential docking to D1 (*green*) for the hexamer (Fig. 7, *E* and *F*).

### *Molecular dynamics of NSF-bound PA may indicate a hinge mechanism*

Molecular dynamics simulations were selectively performed on clusters 3 and 4 (*purple* and *orange*), which are found in the interface between D1 and D2, not overlapping with the D2 ATP-binding site. From each of the two clusters a top pose was filtered using the highest Autodock Vina scoring function score for simulation (Videos S3 and S4). These simulations indicate flexibility between the D1–D2 interface (Fig. 8). These simulations show either an opening or closing of D2 with respect to D1 as demonstrated by overlapping trials. These results further support the mechanism as described in Fig. 9.

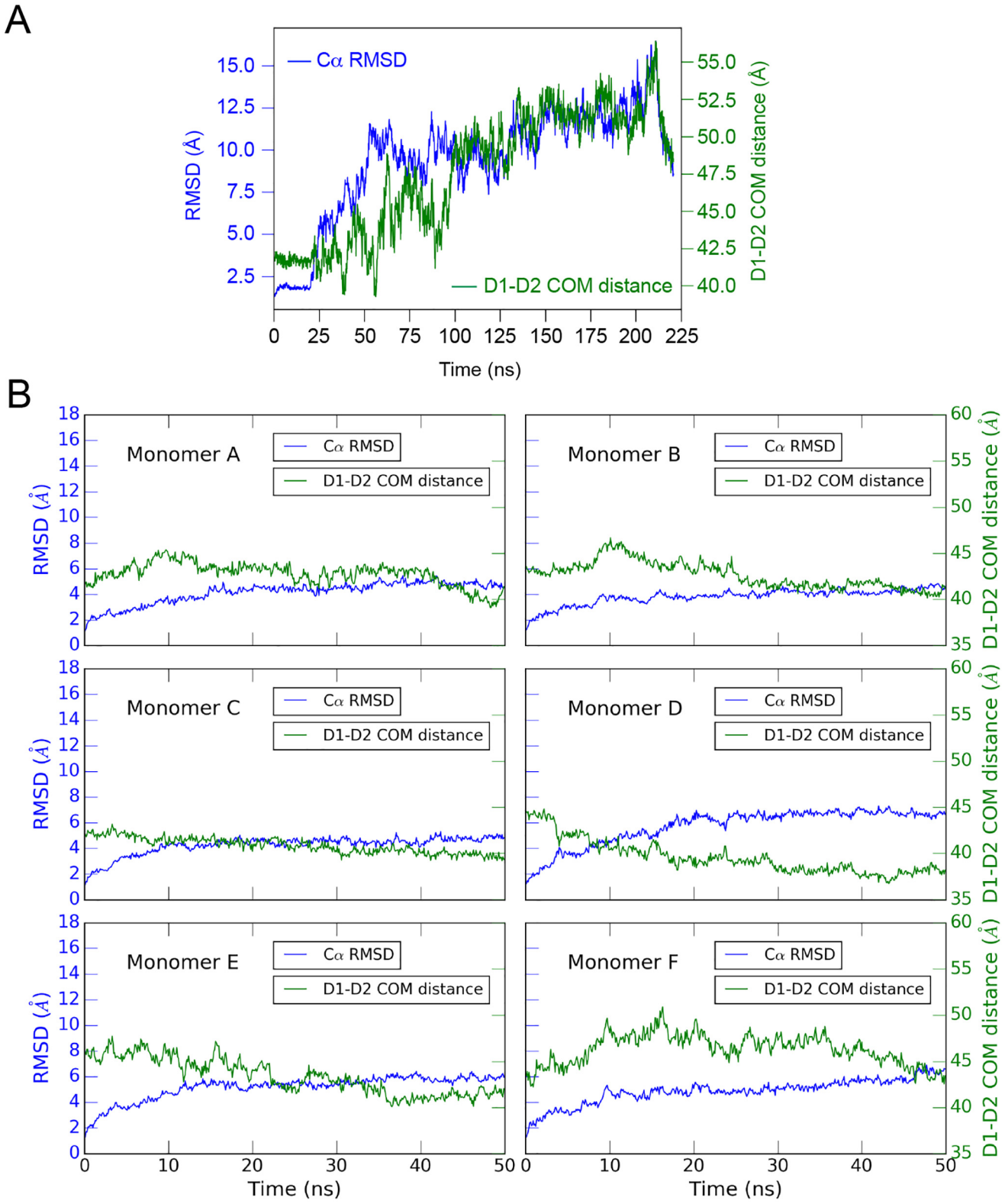


**Figure 5. Computational simulations show large scale conformational change between D1 and D2 subunits of NSF and indicate potential PA-binding regions of NSF.** *A,* D1–D2 monomer undergoes large conformational changes during relaxation. In the first 20 ns, the D1–D2 monomer was equilibrated with a 0.05 kcal/mol/Å$^2$ harmonic restraint on protein Cα atoms. *Blue,* D1–D2 monomer Cα r.m.s. deviation; *green,* center of mass distance between D1 and D2 domains. *B,* D1–D2 r.m.s. deviation of individual protomers within a hexamer are stable throughout equilibration.

## Discussion

Membrane fusion is a necessary process for all eukaryotes, and Sec18/NSF is the only known protein responsible for utilizing energy from ATP to prime SNAREs (3, 4, 8). To achieve compartmental specificity, unique SNARE combinations are utilized by defined organelles as well as smaller transport vesi-

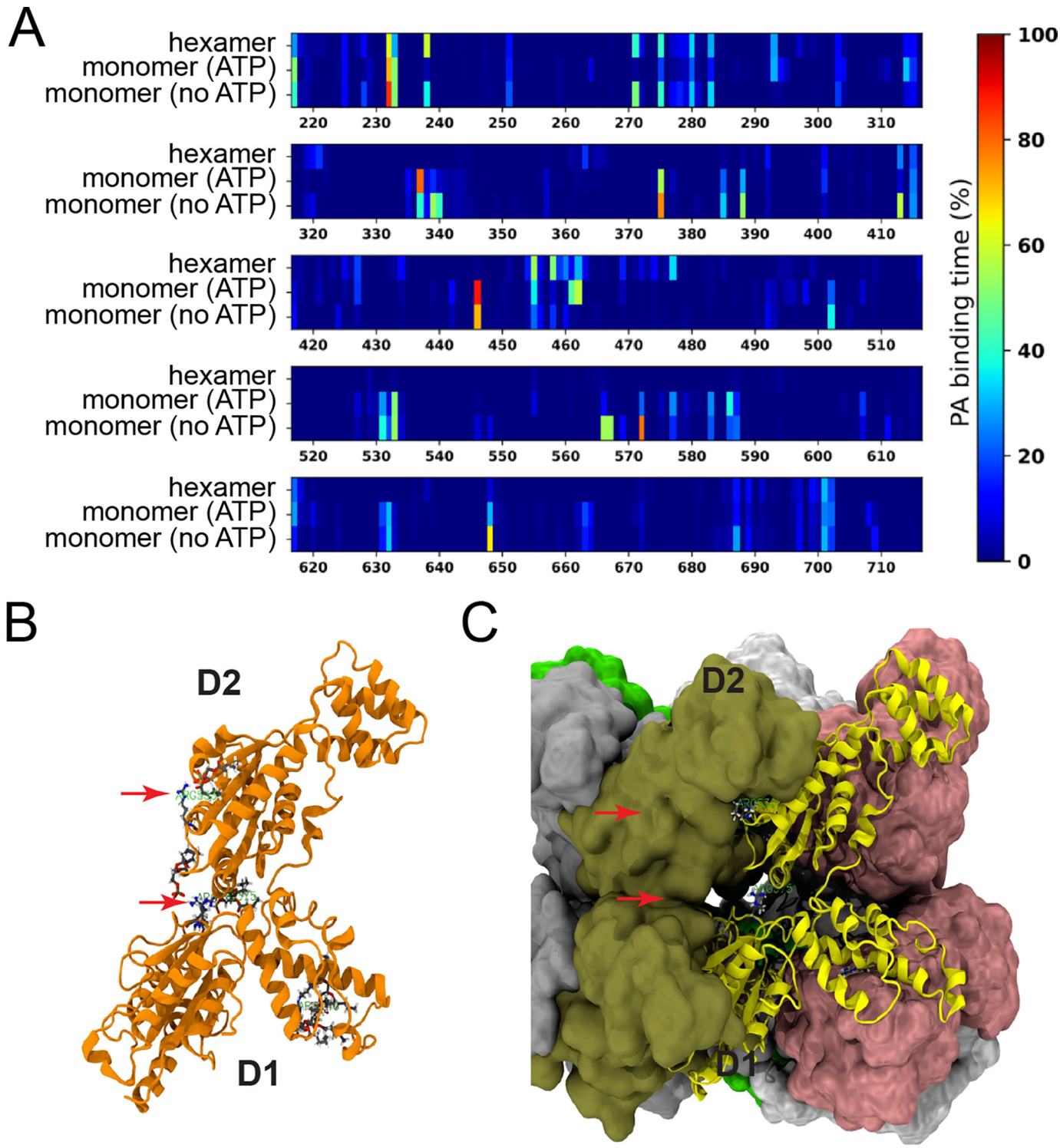


**Figure 6. Flooding of Sec18 with PA.** *A,* protomer chain A from hexamer cryo-EM structure (PDB 3J94) was simulated in short-tailed PA solution (119 mM, 61 PA molecules in a 95 Å × 94 Å × 120 Å water box) for 350 ns with ATP binding and 200 ns without ATP. Binding percentages were measured according to the amount of time a PA molecule was within a hydrogen bonding distance from a given amino acid residue of NSF according to heat map on the *right side* of *A* with residues of NSF indicated on the *x* axis and model flooded on the *y* axis. Both monomer (*B*) and hexamer (*C*) are shown with key residues from *B* indicated on the B monomer and *C* hexamer demonstrating the region of hexamer where residues of monomer showing high binding are located.

cles budding from such organelles (45). Each organelle varies in both size and function, and must contain its own unique combination of protein and lipid factors to allow for specificity in trafficking and membrane-fusion events. Regulation of Sec18/NSF is of special significance due its direct role in maintenance of fusion and compartmentalization throughout the eukaryotic cell. Therefore, it is important to understand the role that regulatory factors have on ubiquitous fusion machinery such as Sec18/NSF to adequately model how specificity and efficiency are balanced and maintained at different locations in the cell.

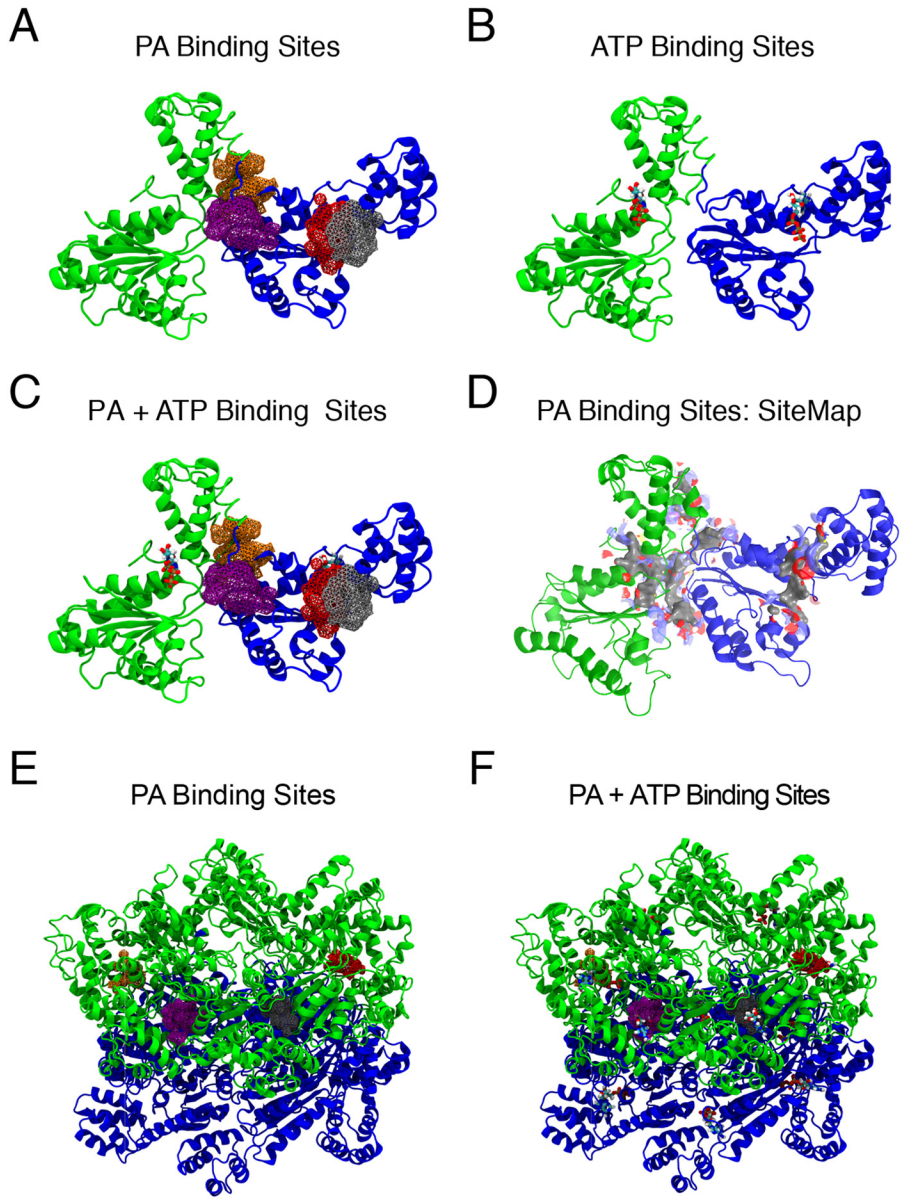


**Figure 7. Ensemble molecular docking and binding site prediction of NSF D1–D2 monomer.** *A,* VMD generated image of NSF monomer of D1 (*green*) and D2 (*blue*) with space filling modeled top clusters ranked in order of the highest docking frequency depicted in *red, gray, purple*, and *orange*, with clusters determined from analysis of AutoDock Vina results. *B,* Schrodinger SiteMap results of the top three site score sites of Schrodinger generated image of NSF monomer D1 (*green*) and D2 (*blue*). *C,* VMD generated image as in Fig. 6*A* including ATP aligned into ATP-binding sites of D1 and D2 domains. *D,* Schrodinger generated image as in Fig. 6*B* including ATP aligned as in Fig. 6*C*. *E,* VMD generated image of NSF hexamer as in Fig. 6*A* including autodock generated cluster analysis. *F,* Schrodinger generated image of NSF hexamer as in Fig. 6*B* including a sitemap generated binding site analysis.

Protein function can be regulated directly through posttranslational modifications or through their interactions with other molecules, including lipids. The vacuole fusion pathway is regulated at various stages by distinct lipids such as phosphoinositides, ergosterol, DAG, and PA (13, 17, 27, 30, 39, 46–52). The priming stage requires the presence of ergosterol, PI(4,5)P2, as well as the conversion of PA to DAG (13, 17, 30, 49).

Previously we found that vacuolar PA sequestered Sec18 from *cis*-SNAREs and that the PA phosphatase Pah1/Lipin1 was required to convert PA to DAG to allow Sec18 dissociation from the membrane and recruitment to SNARE complexes (13). We should also reiterate that the other yeast PA phosphatases have no effect on vacuole fusion, illustrating that this regulation is specific for Pah1 function. Although PA turnover is needed for priming, the presence of the lipid is also required downstream for mechanisms that remain to be characterized. Deletion of *PAH1* or the DAG kinase *DGK1* alters the balance of PA and DAG on vacuole to dramatically affect membrane fusion (17, 27). We thus postulate that enzymatic changes that alter PA levels can in turn shift the equilibrium of Sec18 from a lipid-bound to a SNARE-associated state. Such changes would likely have significant effects on SNARE disassembly and the overall progression of the membrane fusion cascade. That said, any membrane where PA is lacking would be expected to have unfettered access Sec18 to SNAREs.

In this study we demonstrated that Sec18 directly binds PA with high affinity on par with a known PA-binding domain.

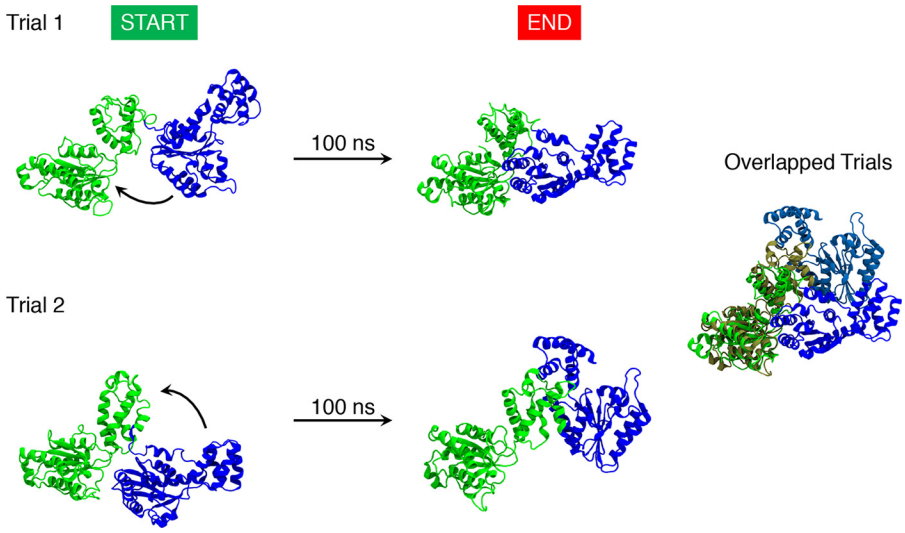


**Figure 8. Short-chain PA MD simulations.** *A,* two separately performed MD simulations based on top poses for two clusters determined from ensemble docking and cluster analysis as described in the legend to Fig. 6, *A* and *B*. MD simulations of each cluster were performed for 100 ns and depicted are two both the starting and ending poses of these simulations extracted from Videos S3 and S4. The combined finishing poses were aligned to D1 of each D1–D2 NSF monomer and the final Overlapped Trials image depicts two separate resting places for the D2 monomer with respect to the D1 monomer in response to short-chain PA.

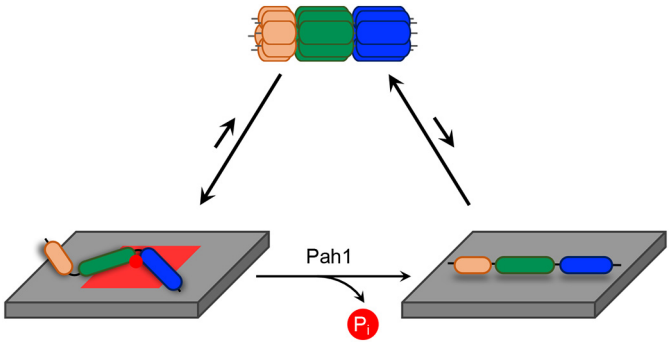


**Figure 9. Model.** A proposed model of mSec18 protomers bound to PA-rich membranes and preventing the formation of functional Sec18 hexamers needed for SNARE priming. Binding PA causes a conformational change in the protomers between the D1 and D2 domains to stabilize membrane association. The PA phosphatase Pah1 hydrolyzes PA to diacylglycerol leading to a conformational reversion that is compatible to dissociation from the membrane and incorporation into a Sec18 holoenzyme.

Moreover, only monomeric Sec18 could bind both long-chain PA in membranes and soluble C8-PA, whereas hexameric was only able to bind C8-PA. This signifies that C8-PA could access PA-binding residues that are blocked in the hexamer to prevent membrane association. Our findings indicate that Sec18 may exist in both a monomeric lipid-bound pool and SNARE-bound hexamers. Because ATP is required for Sec18 hexamerization, we tested PA liposome binding in the presence of ATP. PA-liposome binding by Sec18 was blocked by ATP. We posit that micromolar ATP concentrations may shift the monomeric pool of Sec18 used to a hexameric pool decreasing its affinity for PA. It is worth noting that ATP concentrations in the cytoplasm have been measured in the low millimolar range, which would likely promote spontaneous hexamer formation and maintenance at the vacuole membrane (53). This would suggest Sec18 almost always exists as an active hexamer under physiological conditions. However, we have previously observed disruption of Sec18 activity upon a shift to high levels of PA at the vacuole even in the presence of millimolar concentrations of ATP (13, 17). Additionally, Sec18 association with the vacuole membrane is maintained throughout the fusion cycle, even after it hydrolyzes ATP and allows for the release of Sec17 from the membrane (3). Sec18 binding to the vacuole is also required for membrane association of the fusion factor LMA1, even in the absence of ATP (54). These findings agree with our results and suggest Sec18 may associate with the vacuole membrane in a nucleotide-free state. It is, however, unclear whether some unknown interaction between Sec18 and a fully functional vacuole would limit, or regulate, ATP binding prior to its release upon Pah1 activity. Given our results and these previous findings, we hypothesize that PA at the vacuole membrane stabilizes a nucleotide-free, monomeric form of Sec18 before its recruitment to *cis*-SNAREs. Our evidence for this, however, is indirect and future work should aim to investigate the presence of a monomeric form of Sec18 *in vivo*.

During priming, Sec17/α-SNAP is recognized by Sec18/NSF in an ATP-bound state at D1 before subsequent ATPase activity occurs. We think that Sec18 exists in both lipid-bound and SNARE-bound states and that the presence of ATP at the D1 NBD may determine the state in which the protein primarily exists. Membrane PA may prevent the association of ATP with the D1 NBD locking the protein in an inactive lipid-bound state preventing recruitment to inactive SNARE complexes. This is in line with our data in this study and with observations from previous work (13).

The fact that Sec18 monomer binding to PA liposomes was inhibited at a saturating ATP concentration for the D1 NBD could indicate that the PA-binding site for Sec18 lies near the D1 ATP-binding site. Alternatively, it is possible the conformation of Sec18 in its ATP-bound state shields the protein's unique PA-binding site. The idea that Sec18 binding to PA may not specifically depend on the D1 ATP-binding site was supported by computational flooding experiments performed on both hexamer and monomer in the presence and absence of ATP. Flooding experiments allowed for C8-PA to equilibrate

with NSF monomer, and binding was measured using the length of time a PA molecule resided near a given residue of NSF. Many of the long-term amino acid residues sharing the longest contact time to PA were predictably basic residues, especially lysine and arginine. However, dramatic differences in these residues were not noticed between the ATP and non-ATP simulations. Furthermore, many of the residues with longer PA-binding time were not of importance for PA binding in the hexamer simulation. This result is in corroboration with the high binding affinity of Sec18 monomers to PA liposomes *versus* the hexameric form. This further indicates that the Sec18 monomer and hexamer are differentially regulated. Furthermore, it suggests that PA may influence the formation of the active hexamer by controlling the availability of its inactive monomer at membranes.

We propose that Sec18/NSF PA regulation is achieved by sequestration of its protomers by PA to block the formation of the active hexamer to prevent unchecked priming. Upon binding PA, Sec18/NSF undergoes a significant conformational change that coincides with a reduction in its SNARE priming activity. Thus, PA sequestration can negatively regulate SNARE priming (55). Additionally, it is possible that PA at the site of priming could have a globally positive influence on priming by increasing the local concentration near the site of action. Previous work has shown that PA is necessary for vacuole fusion to occur and is required for Sec18 association with the membrane (56). Although this appears to somewhat contradict our findings presented here, we do not believe this is the case. Unregulated Sec18 activity has previously been shown to be detrimental to vacuole fusion (57–60). Factors such as the PA phosphatase Pah1/Lipin, could thus serve to activate Sec18/NSF only once its activity was required (13, 17). In this way, PA could serve as a temporal regulator of SNARE priming activity and the membrane fusion process as a whole. It is also likely that PA membrane concentrations could differentially affect organelles with distinct lipid content. Depending on the concentration and localization of PA at a given membrane Sec18 sequestration by PA could either play a larger or less prominent role in regulating the priming of SNAREs.

Based on our computational studies, it appears that there are numerous candidate residues that might contribute to Sec18 PA binding. Membrane simulations have been performed (data not shown); however, due to the size and flexibility of Sec18 monomer, long-time scales in the microsecond range may be required to show final binding events sequestering Sec18 to a PA containing membrane. We plan to further probe this binding event using membrane simulations at longer time scales to capture the exact binding event of Sec18 to a PA membrane, and to specifically identify the numerous residues that may be involved.

Because NSF binds PA, we assume that the results from yeast Sec18 will translate to the mammalian system. Our computational results using NSF indicate a conformational change in a novel region of NSF that would not be expected merely from the function of D1 ATPase activity on the N-domain. Our model suggests that PA may influence the ability for NSF to both localize and polymerize to form an active hexameric priming complex. This priming complex could then be differentially regulated at a given organelle utilizing PA as a regulatory lipid, as indicated by our studies of Pah1 at the vacuole (17).

## Experimental procedures

### Reagents

POPA (1-palmitoyl-2-oleoyl-sn-glycero-3-phosphate), POPC (1-palmitoyl-2-oleoyl-*sn*-glycero-3-phosphatidylcholine), POPE (1-palmitoyl-2-oleoyl-*sn*-glycero-3-phosphatidylethanolamine), C8-PA (1,2-dioctanoyl-*sn*-glycero-3-phosphate), C8-DAG (1,2-dioctanoyl-*sn*-glycerol), and C8-PS (1,2-dioctanoyl-*sn*-glycero-3-phospho-L-serine) were purchased from Avanti Polar Lipids (Alabaster, AL) as chloroform stock solutions and stored at −20 °C. CM7 and Ni-NTA (standard and S series) sensor chips, and regeneration buffers (glycine pH 1–3) were procured from GE Healthcare (Buckinghamshire UK). Ni-NTA Atto 488 dye was procured from Sigma. Monolith NT.115 standard treated capillaries for thermophoresis were purchased from Nanotemper (München Germany).

### Plasmid construction

Plasmid for expression of Sec18–$His_8$ was created by amplification of *SEC18* by PCR from genomic DNA of yeast strain DKY6281 using primers containing NdeI and XhoI restriction cut sites (forward: 5′-ACGTACGTCATATGTTCAAGATACCTGGTTTTGG-3′, reverse: 5′-ATCGAATGCTCGAGTGCGGATTGGGTCATCAACT-3′). The PCR product was inserted into pET42a using NdeI and XhoI in-frame with a C-terminal $His_8$ tag sequence under control of a T7 promoter to create pSec18H8.

Plasmid for expression of GST–Sec18 was created using primers containing EcoRI and XhoI restriction cut sites (forward: 5′-ATGCAATGGAATTCATGTTCAAGATACCTGGTTTTGG-3′, reverse: 5′-ATCGAATGCTCGAGTTATGCGGATTGGGTCATCAACT-3′). PCR product was inserted into pParallel GST using EcoRI and XhoI to create pGSTSec18. Plasmid for expression of the GST–N-terminal domain was created in the same way using a different reverse primer (forward: 5′-ATGCAATGGAATTCATGTTCAAGATACCTGGTTTTGG-3′, reverse: 5′-ATCGAATGCTCGAGTCTTCCTTTGAAAAAATTAATTTGTGTTTGTTT-3′) to create pGSTN.

### Protein purification

For purification, pSec18His8 was transformed into Rosetta 2 (DE3) pLysS Competent Cells (Novagen) and Sec18–$His_8$ expression was carried out using autoinducing medium (AIM) (61). Cells were grown in AIM until reaching stationary phase (37 °C, 18 h, shaking) and harvested by centrifugation. Cells were resuspended in lysis buffer (20 mM HEPES, pH 6.8, 300 mM NaCl, 0.1% Triton X-100, 2 mM 2-mercaptoethanol, 20 mM imidazole, 10% glycerol, 1 mM ATP, 1 mM PMSF, and 1× cOmplete Protease Inhibitor Mixture (Roche Applied Science)) and lysed by French press. Lysates were cleared by centrifugation (50,000 × *g*, 20 min, 4 °C) and incubated with Ni-NTA resin (Invitrogen) overnight at 4 °C. Resin was washed with 100 bed volumes of wash buffer (lysis buffer with 50 mM imidazole) before the protein was eluted in 1-ml fractions (lysis buffer with

250 mM imidazole). Protein was concentrated before being run through gel filtration (Superose 6) using size exclusion buffer (20 mM HEPES, pH 6.8, 300 mM NaCl, 1 mM 2-mercaptoethanol, 10% glycerol). Sec18–$His_8$ elutes in two peaks corresponding to monomeric and hexameric pools. Each pool was collected and concentrated before use. For CD experiments, Sec18–$His_8$ was purified using the same approach with different buffer compositions. CD lysis buffer (50 mM phosphate buffer, pH 6.8, 20 mM imidazole, 1 mM PMSF), CD wash buffer (50 mM phosphate buffer, pH 6.8, 50 mM imidazole), CD elution buffer (50 mM phosphate buffer, pH 6.8, 250 mM imidazole), and CD SEC buffer (50 mM phosphate buffer, pH 6.8) were used. GST–Sec18 was purified similarly using Rosetta 2 (DE3) pLysS competent cells transformed with pGSTSec18 but with the following changes. GST lysis buffer (50 mM Tris, pH 8.0, 150 mM NaCl, 5 mM EDTA, 1 mM ATP, 1 mM PMSF, and 1× cOmplete Protease Inhibitor Mixture) was used through the lysis and chromatography wash steps. Protein was eluted with GST elution buffer (20 mM HEPES, pH 7.2, 150 mM NaCl, 10 mM reduced GSH) and dialyzed against 1× HBS, pH 7.2, before being aliquoted and stored at −80 °C. GST-N was purified in the same way using cells transformed with pGST-N. The DEP PA-binding domain from murine Dvl2 was purified as a GST fusion as described (34). Membrane scaffold protein 1D1 (MSP1D1-His) was prepared as described (62). GST-Vam7 and Sec17 were expressed and purified as shown previously (32, 63, 64). Purification of GST-Nyv1(ΔTM) was performed as previously described with minor changes (65). Protein overexpression was carried out in *Escherichia coli* (BL21) using AIM (61). Cells were grown in AIM until reaching stationary phase (37 °C, 18 h, shaking) and harvested by centrifugation. Cells were resuspended in lysis buffer (1× PBS, pH 7.4, 2 mM EDTA, 2 mM DTT, 1 mM PMSF, and 1× cOmplete Protease Inhibitor Mixture (Roche)) and lysed by French press. Lysate was cleared by centrifugation (50,000 × *g*, 20 min, 4 °C) and incubated with GSH-agarose resin (Pierce) overnight at 4 °C. Resin was washed with 100 bed volumes of lysis buffer before the protein was eluted in 1-ml fractions (20 mM HEPES, pH 7.2, 150 mM NaCl, 20 mM GSH). Protein was concentrated before dialysis in 1× HBS, pH 7.2. MBP-sVti1 and MBP-sVam3s were purified as previously described with minor changes (66). Briefly, protein overexpression was carried out in *E. coli* (BL21) using AIM (37 °C, 18 h, shaking). Cells were harvested by centrifugation and resuspended in lysis buffer (20 mM Tris, pH 8.0, 200 mM NaCl, 1 mM PMSF, and 1X cOmplete Protease Inhibitor Mixture (Roche)). Cells were lysed by French press and lysate was cleared by centrifugation (50,000 × *g*, 20 min, 4 °C). Cleared lysate was incubated with amylose resin (New England Biolabs) overnight at 4 °C. Resin was washed with 100 bed volumes of lysis buffer and eluted in 1-ml fractions with elution buffer (lysis buffer with 10 mM maltose). Proteins were concentrated and dialyzed into 1× HBS, pH 7.2.

### *Nanodisc preparation*

Lipid composition of PA nanodiscs consisting of 3.023 μmol of POPC $diC_{16}$, 0.098 μmol of PA $diC_{16}$, and 0.78 μmol of POPE, and PC nanodiscs consisting of 3.121 μmol of POPC $diC_{16}$ and 0.78 μmol of POPE were combined, dried, and desiccated overnight. Lipids were then dissolved in 20 mM sodium deoxycholate in TBS (50 mM Tris-HCl, pH 7.4, 150 mM NaCl, and 0.02% $NaN_3$) and sonicated. MSP1D1 membrane scaffold protein (MSP) was then added in a ratio of 70:1 lipid to protein and detergent was removed with Bio-Beads® SM-2 (Bio-Rad). Nanodiscs were isolated using size exclusion chromatograph and quantified using a NanoDrop and the extinction coefficient of 21,000 liter $mol^{-1}$ $cm^{-1}$ for MSP1D1 (24.66 kDa), and the resultant mg/ml divided by two because there are two MSP proteins per nanodisc (67).

### *Surface plasmon resonance*

SPR measurements were performed on a Biacore T200 instrument equipped with an Ni-NTA chip (68). Approximately 2000 response units of 5% PA nanodiscs were immobilized noncovalently using 1 μM $NiSO_4$ flowed at 10 μl/s followed by a blank buffer injection of HEPES, pH 7.4, 150 mM NaCl (HBS buffer). Injections were performed in HBS buffer at a flow rate of 30 μl/min with an association time of 90 s, dissociation time of 300 s, and binding was measured in relative response units as described (67). Regeneration with EDTA was performed at flow rate 30 μl/s for 120 s using 100 nM EDTA buffer. Proteins were injected using 1:1 dilutions from the highest concentration and steady state was obtained using GE BIAcore T200 evaluation software version 3.0 (BIAevaluate). Proteins were injected using 1:1 dilutions for the Sec18 monomer (3.64 μM, 1,82 μM, 911 nM, and 455 nM), DEP PA-binding domain (57.5, 28.8, 14.4, 7.2, 3.6, and 5.8 μM), and N domain from Sec18 (84.3 μM, 8.4 μM, 4.2 μM, 1.1 μM, 527 nM, and 1.69 μM) with one concentration from each titration run in duplicate. Steady state data were fitted and exported using BiaEvaluate software into GraphPad Prism 7.00 for Windows, GraphPad Software (La Jolla, CA).

### *Microscale thermophoresis*

Thermophoresis measurements were performed using a Monolith NT.115-labeled thermophoresis machine (69). Sec18–$His_8$ was labeled with Ni-NTA Atto 488 according to the manufacturer's protocol mixing 200 nM protein with 100 nM dye and allowing to sit at room temperature for 30 min followed by centrifugation. M.O. Control software was used for operation of MST. Target protein concentrations were 50 nM for all His tag-labeled proteins Sec18 monomer, Sec18 hexamer, PA nanodiscs, and PC nanodiscs. LED excitation power was set to 90% and MST set to high allowing 3 s prior to MST to check for initial fluorescence differences, 25 s for thermophoresis, and 3 s for regeneration after MST off. Analysis was performed using M.O. Affinity Analysis Software as the difference between the initial fluorescence measure in the first 5 s as compared with thermophoresis at 15 s. All measurements were performed in PBS buffer (137 mM NaCl, 2.7 mM KCl, 8 mM $Na_2HPO_4$, and 2 mM $KH_2PO_4$, pH 7.4) without Tween and binding affinity was generated using GraphPad Sigmoidal 4PL fit from points exported from M.O. Affinity Analysis software using $K_D$ Model with target concentration fixed at 50 nM generating bound, unbound, and fraction bound for export to GraphPad to estimate the final $K_D$.

### Limited proteolysis

Cleavage reactions were carried out in proteolysis buffer (20 mM HEPES, pH 7.2, 150 mM NaCl, 2 mM ATP, 2 mM $MgCl_2$). Sec18–$His_8$ (2 $\mu$M) was added to proteolysis buffer and incubated with the indicated lipid concentration on ice for 5 min. Trypsin or thrombin diluted in 1× HBS was added to assay tubes at the indicated concentrations and incubated at 25 °C for 30 min. Cleavage reactions were stopped with the addition of SDS sample buffer containing 1 mM PMSF. Samples were resolved with SDS-PAGE and gels were stained using Coomassie Blue. Gels were destained with methanol/acetic acid solution (50%/7%) and imaged using a ChemiDoc MP Imaging System (Bio-Rad).

### Tryptophan fluorescence spectroscopy

Sec18–$His_8$ (500 nM) was incubated with the indicated concentrations of C8-PA in fluorescence assay buffer (20 mM HEPES, pH 7.2, 150 mM NaCl, 1 mM $MgCl_2$, 1 mM ATP). Lipid dilutions were first prepared in assay buffer and measured for background fluorescence before Sec18–$His_8$ was added and incubated at 25 °C. Intrinsic tryptophan fluorescence measurements were made using a fluorimeter with Peltier temperature control (Agilent Technologies). Samples were excited at 295 nm and the emission spectra were collected from 300 to 400 nm. Samples were measured in a 100-$\mu$l cuvette (Starna Cells). Initial background fluorescence spectra for each lipid concentration were subtracted from final measurements.

### 1,8-ANS fluorescence spectroscopy

ANS binding experiments were carried out in fluorescence assay buffer with 5 $\mu$M ANS (Cayman Chemical). Initial spectra were taken without Sec18–$His_8$ to measure any background fluorescence from buffer or added lipids (excitation 350 nm, emission 390–620 nm). Sec18–$His_8$ diluted in assay conditions was then added to the assay to the indicated concentration and incubated at 25 °C for 5 min before spectra were obtained. Initial background fluorescence spectra for each lipid concentration were subtracted from final measurements.

### Circular dichroism

Monomeric Sec18–$His_8$ purified in phosphate buffer was incubated with and without C8-PA to equilibrium (25 °C, 15 min). Protein concentration used was 5 $\mu$M and lipid concentration used was 100 $\mu$M. CD was measured using a spectropolarimeter (JASCO). All spectra were recorded from 260 to 200 nm at 50 nm $min^{-1}$ and measurements were taken in a 1-mm path length cuvette.

### Differential scanning fluorimetry

Sec18 (2.75 mg/ml) was diluted to a final concentration of 0.11 mg/ml in phosphate buffer containing 1 mM ATP, 1 mM $MgCl_2$, and 4× SYPRO orange dye. Next, 22.5 $\mu$l of this mix was added to a white hard-shell 96-well PCR plate (Bio-Rad), which contained 2.5 $\mu$l of serial dilutions of C8-PA in phosphate buffer. The plates were then sealed with Microseal "B" film (Bio-Rad), and samples were allowed to equilibrate at room temperature for 30 min before beginning the assay. Melting curves were performed using a Bio-Rad CFX Connect real-time detection system. The melt curve protocol was 25 °C for 3 min followed by a 25–90 °C gradient with 0.5 °C increments. Each temperature was held for 10 s and the fluorescence intensity was measured (excitation = 490 nm, emission = 560 nm). The first derivative of the fluorescence readings was used to determine the melting temperature(s) for each condition.

### Preparation of D1–D2 monomer and hexamer models

The D1–D2 monomer model (residues 215–737) was derived from an Cryo-EM structure of ATP-bound NSF complex (PDB 3J94, chain A) (8). Missing residues (335–346, 458–478 in PDB 3J94 (chain A)) were built via homology modeling using the crystal structure of the homologous N–D1 domain of p97 (PDB 1E32) as a template by MODELLER 9.19 (70). The complete D1–D2 hexamer model was prepared (71) using the same PDB 3J94 as the monomer. Missing loops in each monomer were modeled in CHARMM GUI to ensure that no clashes or topological errors exist in the complex structure. *cis*-Peptide bonds in both monomer and hexamer structures were examined and fixed manually using Cispeptide plugin in VMD (72). A further refinement of loops built in the hexamer was performed via MDFF (73).

### Equilibrium MD simulations of D1–D2 monomer and D1–D2 hexamer

The MD simulations were performed with NAMD 2.12 (74) using CHARMM36m force field (75). Langevin dynamics and Langevin piston Nose-Hoover methods (76, 77) were used to maintain constant temperature at 310.15 K and pressure at 1 atm. The long-range electrostatic forces were evaluated using the particle mesh Ewald method (78, 79) with a 1-Å grid spacing. The van der Waals interactions were calculated with a cutoff of 12 Å and a force-based switching scheme after 10 Å. Integration time step was set at 2 fs with SETTLE algorithm (80) applied. VMD 1.9.3 was used for MD trajectory visualization and analysis (81). The D1–D2 monomer model was first equilibrated for 20 ns with harmonic restraints (0.05 kcal/mol/Å2) on protein C$\alpha$ atoms except modeled loops, then followed by 200-ns equilibration without restraints. Furthermore, the D1–D2 hexamer was modeled as for D1–D2 monomer, and simulated for 50 ns without restraints, this was utilized for ensemble docking of PA.

### PA lipids flooding simulations of D1–D2 monomer and D1–D2 hexamer

To demonstrate that hexamerization of sec18 monomer shields PA-binding sites, three independent PA lipids flooding simulations were carried out for: 1) D1–D2 monomer in the absence of ATP molecules; 2) D1–D2 monomer in contacts with four ATP molecules taken from the hexamer structure; and 3) D1–D2 hexamer with all bound ATP molecules. Flooding simulations were prepared by first placing the protein in a PA lipids grid with a grid spacing of 25 Å, where PA lipids were modeled with truncated acyl chains as described in the highly mobile membrane-mimetic model (84, 85) to reassemble the C8-PA experiments as well as avoid micelle formation, followed by solvation and ionization to a NaCl concentration of 150 mM

using the SOLVATE and AUTOIONIZE plugins within VMD (81). The two final D1–D2 monomer systems contained 61 PA lipids in a simulation box of size 95 Å × 94 Å × 120 Å, whereas the D1–D2 hexamer system contained 223 PA lipids in a simulation box of size 188 Å × 187 Å × 133 Å, resulting in a similar PA lipids concentration (~120 mM) in all three systems. D1–D2 monomer systems were simulated for 350 ns each and the hexamer system was simulated for 166 ns, recorded every 20 ps each. Harmonic restraints (0.1 kcal/mol/Å$^2$) were applied on protein C$\alpha$ atoms except for modeled loops as well as the ATP molecules throughout the simulation to prevent conformational changes of the protein or the disassociation of ATP. The PA binding affinity of each amino acid residue was evaluated by calculating the fraction the time that any PA phosphate group atom can be found within 3 Å of this residue (hydrogen atoms not included).

### *Binding site probing of NSF for PA*

To characterize C8-PA and D1–D2 monomer interactions, molecular ensemble docking of PA was done on D1–D2 monomer using AutoDock Vina (42). The previously mentioned equilibrium simulation of D1–D2 was used to fully sample the dynamics of D1–D2 for molecular docking, where snapshots were taken every 1000 ps of the 200-ns trajectory. For each snapshot, an 80 Å × 94 Å × 108 Å grid box was used to fully sample the entire structure. Each snapshot was docked with an exhaustiveness of 10, yielding a total of 2000 PA-docked poses, with the affinities of each pose obtained from the resultant log files. These poses where then clustered using a hybrid K-centers and K-medoids clustering algorithm using the root mean square deviation (r.m.s. deviation) method (43, 82) for which three main clusters where identified. These clusters where then compared with SiteMap (83). Schrodinger SiteMap was used on equilibrated D1–D2 NSF monomer indicating top potential ligand-binding regions of the NSF D1–D2 monomer including shallow binding sites. The same protocol of ensemble docking of PA was done on the 50-ns simulation of hexameric D1–D2, with snapshots taken every 100 ps. A grid box size of 135 Å × 135 Å × 135 Å with a search exhaustiveness of 10 was used, yielding a total of 5000 PA docked poses that were then clustered using the same methodology as the monomer.

### *MD simulations of top poses from ensemble scoring function*

To further probe the effect of C8-PA on D1–D2 conformation, MD simulations were performed as for equilibrium simulation using both NAMD and CHARMM36m force field. Poses from each cluster provided by the ensemble docking from AutoDock Vina with highest scoring function score were selected for simulation. Monomer MD simulations of 100 ns were performed for each of the top poses from each cluster in the same solvent as for flooding containing 150 mM NaCl in water. VMD was used to visualize results and create figures.

### *Data analysis and statistics*

Results are expressed as the mean ± S.E. Experimental replicates ($n$) are defined as the number of separate experiments with different batches of protein, liposomes, and nanodiscs. Where appropriate, significant differences were calculated using two-tailed unpaired $t$-tests. $p$ values ≤0.05 were considered significant.

*Author contributions*—M. L. S., R. P. S., A. S. A., Z. Z., M. L., E. T., and R. A. F. conceptualization; M. L. S., R. P. S., A. S. A., L. R. H., Z. Z., M. L., J. L. J., and R. A. F. data curation; M. L. S., R. P. S., A. S. A., L. R. H., Z. Z., M. L., J. L. J., E. T., and R. A. F. formal analysis; M. L. S. and R. P. S. validation; M. L. S., R. P. S., A. S. A., L. R. H., Z. Z., M. L., J. L. J., and R. A. F. investigation; M. L. S., R. P. S., A. S. A., L. R. H., Z. Z., M. L., J. L. J., E. T., and R. A. F. methodology; M. L. S., R. P. S., A. S. A., and R. A. F. writing-original draft; M. L. S. and R. P. S. writing-review and editing; E. T. and R. A. F. funding acquisition; R. A. F. resources; R. A. F. supervision; R. A. F. project administration.

*Acknowledgments—We thank Drs. Martin Gruebele, Shahar Sukenik, Susan Martinis, and Zach Dayu for technical advice. Computational resources were provided by XSEDE (XSEDE MCA06N060) and Blue Waters (ACI-1440026). SPR was aided by the help of Dr. Jermaine Jenkins at the University of Rochester Structural Biology & Biophysics Facility with support from National Institutes of Health NCRR Grant 1S10 RR027241, National Institutes of Health NIAID Grant P30AI078498, and the University of Rochester School of Medicine and Dentistry.*

## References

1. Jahn, R., and Südhof, T. C. (1999) Membrane fusion and exocytosis. *Annu. Rev. Biochem.* **68,** 863–911 CrossRef Medline
2. Jahn, R., Lang, T., and Südhof, T. C. (2003) Membrane fusion. *Cell* **112,** 519–533 CrossRef Medline
3. Mayer, A., Wickner, W., and Haas, A. (1996) Sec18p (NSF)-driven release of Sec17p (α-SNAP) can precede docking and fusion of yeast vacuoles. *Cell* **85,** 83–94 CrossRef Medline
4. Ryu, J. K., Min, D., Rah, S. H., Kim, S. J., Park, Y., Kim, H., Hyeon, C., Kim, H. M., Jahn, R., and Yoon, T. Y. (2015) Spring-loaded unraveling of a single SNARE complex by NSF in one round of ATP turnover. *Science* **347,** 1485–1489 CrossRef Medline
5. Chang, L. F., Chen, S., Liu, C. C., Pan, X., Jiang, J., Bai, X. C., Xie, X., Wang, H. W., and Sui, S. F. (2012) Structural characterization of full-length NSF and 20S particles. *Nat. Struct. Mol. Biol.* **19,** 268–275 CrossRef Medline
6. Söllner, T., Bennett, M. K., Whiteheart, S. W., Scheller, R. H., and Rothman, J. E. (1993) A protein assembly-disassembly pathway *in vitro* that may correspond to sequential steps of synaptic vesicle docking, activation, and fusion. *Cell* **75,** 409–418 CrossRef Medline
7. Wilson, D. W., Whiteheart, S. W., Wiedmann, M., Brunner, M., and Rothman, J. E. (1992) A multisubunit particle implicated in membrane fusion. *J. Cell Biol.* **117,** 531–538 CrossRef Medline
8. Zhao, M., Wu, S., Zhou, Q., Vivona, S., Cipriano, D. J., Cheng, Y., and Brunger, A. T. (2015) Mechanistic insights into the recycling machine of the SNARE complex. *Nature* **518,** 61–67 CrossRef Medline
9. Block, M. R., Glick, B. S., Wilcox, C. A., Wieland, F. T., and Rothman, J. E. (1988) Purification of an *N*-ethylmaleimide-sensitive protein catalyzing vesicular transport. *Proc. Natl. Acad. Sci. U.S.A.* **85,** 7852–7856 CrossRef Medline
10. Fleming, K. G., Hohl, T. M., Yu, R. C., Müller, S. A., Wolpensinger, B., Engel, A., Engelhardt, H., Brünger, A. T., Söllner, T. H., and Hanson, P. I. (1998) A revised model for the oligomeric state of the *N*-ethylmaleimide-sensitive fusion protein, NSF. *J. Biol. Chem.* **273,** 15675–15681 CrossRef Medline
11. Whiteheart, S. W., Rossnagel, K., Buhrow, S. A., Brunner, M., Jaenicke, R., and Rothman, J. E. (1994) *N*-Ethylmaleimide-sensitive fusion protein: a trimeric ATPase whose hydrolysis of ATP is required for membrane fusion. *J. Cell Biol.* **126,** 945–954 CrossRef Medline
12. Manifava, M., Thuring, J. W., Lim, Z. Y., Packman, L., Holmes, A. B., and Ktistakis, N. T. (2001) Differential binding of traffic-related proteins to

phosphatidic acid- or phosphatidylinositol (4,5)-bisphosphate-coupled affinity reagents. *J. Biol. Chem.* **276,** 8987–8994 CrossRef Medline
13. Starr, M. L., Hurst, L. R., and Fratti, R. A. (2016) Phosphatidic acid sequesters Sec18p from cis-SNARE complexes to inhibit priming. *Traffic* **17,** 1091–1109 CrossRef Medline
14. Liu, S., Wilson, K. A., Rice-Stitt, T., Neiman, A. M., and McNew, J. A. (2007) *In vitro* fusion catalyzed by the sporulation-specific t-SNARE light-chain Spo20p is stimulated by phosphatidic acid. *Traffic* **8,** 1630–1643 CrossRef Medline
15. Nakanishi, H., Morishita, M., Schwartz, C. L., Coluccio, A., Engebrecht, J., and Neiman, A. M. (2006) Phospholipase D and the SNARE Sso1p are necessary for vesicle fusion during sporulation in yeast. *J. Cell Sci.* **119,** 1406–1415 CrossRef Medline
16. Rogasevskaia, T. P., and Coorssen, J. R. (2015) The role of phospholipase D in regulated exocytosis. *J. Biol. Chem.* **290,** 28683–28696 CrossRef Medline
17. Sasser, T., Qiu, Q. S., Karunakaran, S., Padolina, M., Reyes, A., Flood, B., Smith, S., Gonzales, C., and Fratti, R. A. (2012) Yeast lipin 1 orthologue pah1p regulates vacuole homeostasis and membrane fusion. *J. Biol. Chem.* **287,** 2221–2236 CrossRef Medline
18. Caumont, A. S., Galas, M. C., Vitale, N., Aunis, D., and Bader, M. F. (1998) Regulated exocytosis in chromaffin cells: translocation of ARF6 stimulates a plasma membrane-associated phospholipase D. *J. Biol. Chem.* **273,** 1373–1379 CrossRef Medline
19. Vitale, N., Caumont, A. S., Chasserot-Golaz, S., Du, G., Wu, S., Sciorra, V. A., Morris, A. J., Frohman, M. A., and Bader, M. F. (2001) Phospholipase D1: a key factor for the exocytotic machinery in neuroendocrine cells. *EMBO J.* **20,** 2424–2434 CrossRef Medline
20. Vitale, N., Chasserot-Golaz, S., Bailly, Y., Morinaga, N., Frohman, M. A., and Bader, M. F. (2002) Calcium-regulated exocytosis of dense-core vesicles requires the activation of ADP-ribosylation factor (ARF)6 by ARF nucleotide binding site opener at the plasma membrane. *J. Cell Biol.* **159,** 79–89 CrossRef Medline
21. Zeniou-Meyer, M., Zabari, N., Ashery, U., Chasserot-Golaz, S., Haeberlé, A. M., Demais, V., Bailly, Y., Gottfried, I., Nakanishi, H., Neiman, A. M., Du, G., Frohman, M. A., Bader, M. F., and Vitale, N. (2007) Phospholipase D1 production of phosphatidic acid at the plasma membrane promotes exocytosis of large dense-core granules at a late stage. *J. Biol. Chem.* **282,** 21746–21757 CrossRef Medline
22. Huang, P., Altshuller, Y. M., Hou, J. C., Pessin, J. E., and Frohman, M. A. (2005) Insulin-stimulated plasma membrane fusion of Glut4 glucose transporter-containing vesicles is regulated by phospholipase D1. *Mol. Biol. Cell* **16,** 2614–2623 CrossRef Medline
23. Kooijman, E. E., Chupin, V., Fuller, N. L., Kozlov, M. M., de Kruijff, B., Burger, K. N., and Rand, P. R. (2005) Spontaneous curvature of phosphatidic acid and lysophosphatidic acid. *Biochemistry* **44,** 2097–2102 CrossRef Medline
24. Lam, A. D., Tryoen-Toth, P., Tsai, B., Vitale, N., and Stuenkel, E. L. (2008) SNARE-catalyzed fusion events are regulated by Syntaxin1A-lipid interactions. *Mol. Biol. Cell* **19,** 485–497 CrossRef Medline
25. Nakanishi, H., de los Santos, P., and Neiman, A. M. (2004) Positive and negative regulation of a SNARE protein by control of intracellular localization. *Mol. Biol. Cell* **15,** 1802–1815 CrossRef Medline
26. Churchward, M. A., Rogasevskaia, T., Brandman, D. M., Khosravani, H., Nava, P., Atkinson, J. K., and Coorssen, J. R. (2008) Specific lipids supply critical negative spontaneous curvature: an essential component of native $Ca^{2+}$-triggered membrane fusion. *Biophys. J.* **94,** 3976–3986 CrossRef Medline
27. Miner, G. E., Starr, M. L., Hurst, L. R., and Fratti, R. A. (2017) Deleting the DAG kinase Dgk1 augments yeast vacuole fusion through increased Ypt7 activity and altered membrane fluidity. *Traffic* **18,** 315–329 CrossRef Medline
28. Zhao, M., and Brunger, A. T. (2016) Recent advances in deciphering the structure and molecular mechanism of the $AAA^+$ ATPase *N*-ethylmaleimide-sensitive factor (NSF). *J. Mol. Biol.* **428,** 1912–1926 CrossRef Medline
29. Horchani, H., de Saint-Jean, M., Barelli, H., and Antonny, B. (2014) Interaction of the Spo20 membrane-sensor motif with phosphatidic acid and other anionic lipids, and influence of the membrane environment. *PLoS ONE* **9,** e113484 CrossRef Medline
30. Mayer, A., Scheglmann, D., Dove, S., Glatz, A., Wickner, W., and Haas, A. (2000) Phosphatidylinositol 4,5-bisphosphate regulates two steps of homotypic vacuole fusion. *Mol. Biol. Cell* **11,** 807–817 CrossRef Medline
31. Matveeva, E. A., He, P., and Whiteheart, S. W. (1997) *N*-Ethylmaleimide-sensitive fusion protein contains high and low affinity ATP-binding sites that are functionally distinct. *J. Biol. Chem.* **272,** 26413–26418 CrossRef Medline
32. Fratti, R. A., Collins, K. M., Hickey, C. M., and Wickner, W. (2007) Stringent 3Q: 1R composition of the SNARE 0-layer can be bypassed for fusion by compensatory SNARE mutation or by lipid bilayer modification. *J. Biol. Chem.* **282,** 14861–14867 CrossRef Medline
33. Jun, Y., Thorngren, N., Starai, V. J., Fratti, R. A., Collins, K., and Wickner, W. (2006) Reversible, cooperative reactions of yeast vacuole docking. *EMBO J.* **25,** 5260–5269 CrossRef Medline
34. Capelluto, D. G., Zhao, X., Lucas, A., Lemkul, J. A., Xiao, S., Fu, X., Sun, F., Bevan, D. R., and Finkielstein, C. V. (2014) Biophysical and molecular-dynamics studies of phosphatidic acid binding by the Dvl-2 DEP domain. *Biophys. J.* **106,** 1101–1111 CrossRef Medline
35. Heyduk, T., and Lee, J. C. (1989) *Escherichia coli* cAMP receptor protein: evidence for three protein conformational states with different promoter binding affinities. *Biochemistry* **28,** 6914–6924 CrossRef Medline
36. Roberts, R. L., Barbieri, M. A., Pryse, K. M., Chua, M., Morisaki, J. H., and Stahl, P. D. (1999) Endosome fusion in living cells overexpressing GFP-rab5. *J. Cell Sci.* **112,** 3667–3675 Medline
37. Lenzen, C. U., Steinmann, D., Whiteheart, S. W., and Weis, W. I. (1998) Crystal structure of the hexamerization domain of *N*-ethylmaleimide-sensitive fusion protein. *Cell* **94,** 525–536 CrossRef Medline
38. Yu, R. C., Hanson, P. I., Jahn, R., and Brünger, A. T. (1998) Structure of the ATP-dependent oligomerization domain of *N*-ethylmaleimide sensitive factor complexed with ATP. *Nat. Struct. Biol.* **5,** 803–811 CrossRef Medline
39. Miner, G. E., Starr, M. L., Hurst, L. R., Sparks, R. P., Padolina, M., and Fratti, R. A. (2016) The central polybasic region of the soluble SNARE (soluble *N*-ethylmaleimide-sensitive factor attachment protein receptor) Vam7 affects binding to phosphatidylinositol 3-phosphate by the PX (Phox homology) domain. *J. Biol. Chem.* **291,** 17651–17663 CrossRef Medline
40. Hew, K., Dahlroth, S. L., Veerappan, S., Pan, L. X., Cornvik, T., and Nordlund, P. (2015) Structure of the Varicella zoster virus thymidylate synthase establishes functional and structural similarities as the human enzyme and potentiates itself as a target of brivudine. *PLoS ONE* **10,** e0143947 CrossRef Medline
41. Vollrath, F., Hawkins, N., Porter, D., Holland, C., and Boulet-Audet, M. (2014) Differential scanning fluorimetry provides high throughput data on silk protein transitions. *Sci. Rep.* **4,** 5625 Medline
42. Trott, O., and Olson, A. J. (2010) AutoDock Vina: improving the speed and accuracy of docking with a new scoring function, efficient optimization, and multithreading. *J. Comput. Chem.* **31,** 455–461 Medline
43. Beauchamp, K. A., Bowman, G. R., Lane, T. J., Maibaum, L., Haque, I. S., and Pande, V. S. (2011) MSMBuilder2: modeling conformational dynamics at the picosecond to millisecond scale. *J. Chem. Theory Comput.* **7,** 3412–3419 CrossRef Medline
44. Friesner, R. A., Murphy, R. B., Repasky, M. P., Frye, L. L., Greenwood, J. R., Halgren, T. A., Sanschagrin, P. C., and Mainz, D. T. (2006) Extra precision glide: docking and scoring incorporating a model of hydrophobic enclosure for protein-ligand complexes. *J. Med. Chem.* **49,** 6177–6196 CrossRef Medline
45. Jahn, R., and Scheller, R. H. (2006) SNAREs: engines for membrane fusion. *Nat. Rev. Mol. Cell Biol.* **7,** 631–643 CrossRef Medline
46. Boeddinghaus, C., Merz, A. J., Laage, R., and Ungermann, C. (2002) A cycle of Vam7p release from and PtdIns 3-P-dependent rebinding to the yeast vacuole is required for homotypic vacuole fusion. *J. Cell Biol.* **157,** 79–89 CrossRef Medline
47. Fratti, R. A., Jun, Y., Merz, A. J., Margolis, N., and Wickner, W. (2004) Interdependent assembly of specific regulatory lipids and membrane fu-

sion proteins into the vertex ring domain of docked vacuoles. *J. Cell Biol.* **167,** 1087–1098 CrossRef Medline
48. Jun, Y., Fratti, R. A., and Wickner, W. (2004) Diacylglycerol and its formation by phospholipase C regulate Rab- and SNARE-dependent yeast vacuole fusion. *J. Biol. Chem.* **279,** 53186–53195 CrossRef Medline
49. Kato, M., and Wickner, W. (2001) Ergosterol is required for the Sec18/ATP-dependent priming step of homotypic vacuole fusion. *EMBO J.* **20,** 4035–4040 CrossRef Medline
50. Karunakaran, S., Sasser, T., Rajalekshmi, S., and Fratti, R. A. (2012) SNAREs, HOPS, and regulatory lipids control the dynamics of vacuolar actin during homotypic fusion. *J. Cell Sci.* **125,** 1683–1692 CrossRef Medline
51. Karunakaran, S., and Fratti, R. (2013) The lipid composition and physical properties of the yeast vacuole affect the hemifusion-fusion transition. *Traffic* **14,** 650–662 CrossRef Medline
52. Stroupe, C., Collins, K. M., Fratti, R. A., and Wickner, W. (2006) Purification of active HOPS complex reveals its affinities for phosphoinositides and the SNARE Vam7p. *EMBO J.* **25,** 1579–1589 CrossRef Medline
53. Ozalp, V. C., Pedersen, T. R., Nielsen, L. J., and Olsen, L. F. (2010) Time-resolved measurements of intracellular ATP in the yeast *Saccharomyces cerevisiae* using a new type of nanobiosensor. *J. Biol. Chem.* **285,** 37579–37588 CrossRef Medline
54. Xu, Z., Sato, K., and Wickner, W. (1998) LMA1 binds to vacuoles at Sec18p (NSF), transfers upon ATP hydrolysis to a t-SNARE (Vam3p) complex, and is released during fusion. *Cell* **93,** 1125–1134 CrossRef Medline
55. Yavuz, H., Kattan, I., Hernandez, J. M., Hofnagel, O., Witkowska, A., Raunser, S., Walla, P. J., and Jahn, R. (2018) Arrest of *trans*-SNARE zippering uncovers loosely and tightly docked intermediates in membrane fusion. *J. Biol. Chem.* **293,** 8645–8655 CrossRef Medline
56. Mima, J., and Wickner, W. (2009) Complex lipid requirements for SNARE- and SNARE chaperone-dependent membrane fusion. *J. Biol. Chem.* **284,** 27114–27122 CrossRef Medline
57. Lobingier, B. T., Nickerson, D. P., Lo, S. Y., and Merz, A. J. (2014) SM proteins Sly1 and Vps33 co-assemble with Sec17 and SNARE complexes to oppose SNARE disassembly by Sec18. *Elife* **3,** e02272 CrossRef Medline
58. Mima, J., Hickey, C. M., Xu, H., Jun, Y., and Wickner, W. (2008) Reconstituted membrane fusion requires regulatory lipids, SNAREs and synergistic SNARE chaperones. *EMBO J.* **27,** 2031–2042 CrossRef Medline
59. Stroupe, C., Hickey, C. M., Mima, J., Burfeind, A. S., and Wickner, W. (2009) Minimal membrane docking requirements revealed by reconstitution of Rab GTPase-dependent membrane fusion from purified components. *Proc. Natl. Acad. Sci. U.S.A.* **106,** 17626–17633 CrossRef Medline
60. Ungermann, C., and Langosch, D. (2005) Functions of SNAREs in intracellular membrane fusion and lipid bilayer mixing. *J. Cell Sci.* **118,** 3819–3828 CrossRef Medline
61. Studier, F. W. (2014) Stable expression clones and auto-induction for protein production in *E. coli*. *Methods Mol. Biol.* **1091,** 17–32 CrossRef Medline
62. Denisov, I. G., Grinkova, Y. V., Lazarides, A. A., and Sligar, S. G. (2004) Directed self-assembly of monodisperse phospholipid bilayer Nanodiscs with controlled size. *J. Am. Chem. Soc.* **126,** 3477–3487 CrossRef Medline
63. Haas, A., and Wickner, W. (1996) Homotypic vacuole fusion requires Sec17p (yeast α-SNAP) and Sec18p (yeast NSF). *EMBO J.* **15,** 3296–3305 CrossRef Medline
64. Fratti, R. A., and Wickner, W. (2007) Distinct targeting and fusion functions of the PX and SNARE domains of yeast vacuolar Vam7p. *J. Biol. Chem.* **282,** 13133–13138 CrossRef Medline
65. Thorngren, N., Collins, K. M., Fratti, R. A., Wickner, W., and Merz, A. J. (2004) A soluble SNARE drives rapid docking, bypassing ATP and Sec17/18p for vacuole fusion. *EMBO J.* **23,** 2765–2776 CrossRef Medline
66. Zick, M., and Wickner, W. (2013) The tethering complex HOPS catalyzes assembly of the soluble SNARE Vam7 into fusogenic trans-SNARE complexes. *Mol. Biol. Cell* **24,** 3746–3753 CrossRef Medline
67. Sparks, R. P., Jenkins, J. L., Miner, G. E., Wang, Y., Guida, W. C., Sparks, C. E., Fratti, R. A., and Sparks, J. D. (2016) Phosphatidylinositol (3,4,5)-trisphosphate binds to sortilin and competes with neurotensin: implications for very low density lipoprotein binding. *Biochem. Biophys. Res. Commun.* **479,** 551–556 CrossRef Medline
68. Sparks, R. P., Jenkins, J. L., and Fratti, R. (2019) Use of surface plasmon resonance (SPR) to determine binding affinities and kinetic parameters between components important in fusion machinery. *Methods Mol. Biol.* **1860,** 199–210 CrossRef Medline
69. Sparks, R. P., and Fratti, R. (2019) Use of microscale thermophoresis (MST) to measure binding affinities of components of the fusion machinery. *Methods Mol. Biol.* **1860,** 191–198 CrossRef Medline
70. Sali, A., and Blundell, T. L. (1993) Comparative protein modelling by satisfaction of spatial restraints. *J. Mol. Biol.* **234,** 779–815 CrossRef Medline
71. Jo, S., Cheng, X., Islam, S. M., Huang, L., Rui, H., Zhu, A., Lee, H. S., Qi, Y., Han, W., Vanommeslaeghe, K., MacKerell, A. D., Jr., Roux, B., and Im, W. (2014) CHARMM-GUI PDB manipulator for advanced modeling and simulations of proteins containing nonstandard residues. *Adv. Protein Chem. Struct. Biol.* **96,** 235–265 CrossRef Medline
72. Schreiner, E., Trabuco, L. G., Freddolino, P. L., and Schulten, K. (2011) Stereochemical errors and their implications for molecular dynamics simulations. *BMC Bioinformatics* **12,** 190 CrossRef Medline
73. Trabuco, L. G., Villa, E., Mitra, K., Frank, J., and Schulten, K. (2008) Flexible fitting of atomic structures into electron microscopy maps using molecular dynamics. *Structure* **16,** 673–683 CrossRef Medline
74. Phillips, J. C., Braun, R., Wang, W., Gumbart, J., Tajkhorshid, E., Villa, E., Chipot, C., Skeel, R. D., Kalé, L., and Schulten, K. (2005) Scalable molecular dynamics with NAMD. *J. Comput. Chem.* **26,** 1781–1802 CrossRef Medline
75. Huang, J., Rauscher, S., Nawrocki, G., Ran, T., Feig, M., de Groot, B. L., Grubmüller, H., and MacKerell, A. D. (2017) CHARMM36m: an improved force field for folded and intrinsically disordered proteins. *Nat. Methods* **14,** 71–73 CrossRef Medline
76. Feller, S. E., Zhang, Y., Pastor, R. W., and Brooks, B. R. (1995) Constant pressure molecular dynamics simulation: the Langevin piston method. *J. Chem. Phys.* **103,** 4613–4621 CrossRef
77. Martyna, G. J., Tobias, D. J., and Klein, M. L. (1994) Constant pressure molecular dynamics algorithms. *J. Chem. Phys.* **101,** 4177–4189 CrossRef
78. Darden, T., York, D., and Pedersen, L. G. (1993) Particle mesh Ewald: an N·log(N) method for Ewald sums in large systems. *J. Chem. Phys.* **98,** 10089–10092 CrossRef
79. Essmann, U., Perera, L., Berkowitz, M. L., Darden, T., Lee, H., and Pedersen, L. G. (1995) A smooth particle mesh Ewald: an N·log(N) method for Ewald sums in large systems. *J. Chem. Phys.* **103,** 8577–8593 CrossRef
80. Miyamoto, S., and Kollman, P. A. (1992) SETTLE: an analytical version of the SHAKE and RATTLE algorithm for rigid water molecules. *J. Comput. Chem.* **13,** 952–962 CrossRef
81. Humphrey, W., Dalke, A., and Schulten, K. (1996) VMD: visual molecular dynamics. *J. Mol. Graphics* **14,** 22–28
82. Pande, V. S., Beauchamp, K., and Bowman, G. R. (2010) Everything you wanted to know about Markov state models but were afraid to ask. *Methods* **52,** 99–105 CrossRef Medline
83. Halgren, T. A. (2009) Identifying and characterizing binding sites and assessing druggability. *J. Chem. Inf. Model* **49,** 377–389 CrossRef Medline
84. Qi, Y., Cheng, X., Lee, J., Vermaas, J. V., Pogorelov, T. V., Tajkhorshid, E., Park, S., Klauda, J. B., and Im, W. (2015) CHARMM-GUI HMMM builder for membrane simulations with the highly mobile membrane-mimetic model. *Biophys. J.* **109,** 2012–2022 CrossRef Medline
85. Vermaas, J. V., and Tajkhorshid, E. (2017) Differential membrane binding mechanics of synaptotagmin isoforms observed in atomic detail. *Biochemistry* **56,** 281–293 CrossRef Medline

# Phosphatidic acid induces conformational changes in Sec18 protomers that prevent SNARE priming

Matthew L. Starr, Robert P. Sparks, Andres S. Arango, Logan R. Hurst, Zhiyu Zhao, Muyun Lihan, Jermaine L. Jenkins, Emad Tajkhorshid and Rutilio A. Fratti

*J. Biol. Chem. 2019, 294:3100-3116.*
*doi: 10.1074/jbc.RA118.006552 originally published online January 7, 2019*